J. Fluid Mech. (2019), *vol.* 875, *pp.* 974–1003.
doi:10.1017/jfm.2019.531

Small-scale two-dimensional turbulence shaped by bulk viscosity

Emile Touber†

Department of Mechanical Engineering, Imperial College London, London SW7 2AZ, UK

(Received 8 October 2018; revised 29 April 2019; accepted 26 June 2019;
first published online 26 July 2019)

Bulk-to-shear viscosity ratios of three orders of magnitude are often reported in carbon dioxide but are always neglected when predicting aerothermal loads in external (Mars exploration) or internal (turbomachinery, heat exchanger) turbulent flows. The recent (and first) numerical investigations of that matter suggest that the solenoidal turbulence kinetic energy is in fact well predicted despite this seemingly arbitrary simplification. The present work argues that such a conclusion may reflect limitations from the choice of configuration rather than provide a definite statement on the robustness of kinetic-energy transfers to the use of Stokes' hypothesis. Two distinct asymptotic regimes (Euler–Landau and Stokes–Newton) in the eigenmodes of the Navier–Stokes equations are identified. In the Euler–Landau regime, the one captured by earlier studies, acoustic and entropy waves are damped by transport coefficients and the dilatational kinetic energy is dissipated, even more rapidly for high bulk-viscosity fluids and/or forcing frequencies. If the kinetic energy is initially or constantly injected through solenoidal motions, effects on the turbulence kinetic energy remain minor. However, in the Stokes–Newton regime, diffused bulk compressions and advected isothermal compressions are found to prevail and promote small-scale enstrophy via vorticity–dilatation correlations. In the absence of bulk viscosity, the transition to the Stokes–Newton regime occurs within the dissipative scales and is not observed in practice. In contrast, at high bulk viscosities, the Stokes–Newton regime can be made to overlap with the inertial range and disrupt the enstrophy at small scales, which is then dissipated by friction. Thus, flows with substantial inertial ranges and large bulk-to-shear viscosity ratios should experience enhanced transfers to small-scale solenoidal kinetic energy, and therefore faster dissipation rates leading to modifications of the heat-transfer properties. Observing numerically such transfers is still prohibitively expensive, and the present simulations are restricted to two-dimensional turbulence. However, the theory laid here offers useful guidelines to design experimental studies to track the Stokes–Newton regime and associated modifications of the turbulence kinetic energy, which are expected to persist in three-dimensional turbulence.

Key words: gas dynamics, compressible turbulence, Navier–Stokes equations

† Email address for correspondence: e.touber@imperial.ac.uk

1. Introduction

High speed and turbulent flows of carbon dioxide occur in a variety of applications, as a working fluid in compressors for electricity production (Rinaldi, Pecnik & Colonna 2015), as a solvent in rapid expansion processes for drug manufacturing (Phillips & Stella 1993) or as the ambient gas acting on a spacecraft (Wright *et al.* 2010). The ability to accurately predict aerothermal loads or turbulent mixing is critical to the success of such applications. Yet, current continuum-medium models (e.g. Navier–Stokes equations) are based on the assumption that the bulk viscosity can be set to zero (as originally proposed by Stokes (1845)), despite evidences that carbon dioxide can exhibit bulk- to shear-viscosity ratios of more than three orders of magnitude (see Jaeger, Matar & Müller (2018), for a recent example). It is therefore not surprising that the role played by bulk viscosity in freely evolving (Pan & Johnsen 2017; Boukharfane 2018) and wall-bounded (Sciacovelli, Cinnella & Gloerfelt 2017; Szemberg O'Connor 2018) turbulence is gaining interest (this is also true in laminar and shocked flows, see Cramer & Bahmani (2014), Kosuge & Aoki (2018), for example, which are beyond the scope of this paper). More surprising however are their early findings that the solenoidal turbulence kinetic energy appears unaffected by the bulk viscosity. Is the use of Stokes' hypothesis in turbulent flows really a tenable approach?

1.1. *Newtonian fluids and the bulk viscosity*

The stress tensor, $\boldsymbol{T}$, of any substance modelled as a continuum medium obeying the Newtonian-fluid assumptions may be expressed as (see chapter 5 of Aris (1989), for details),

$$\boldsymbol{T} = -p\,\boldsymbol{I} + 2\mu\,\boldsymbol{D}^{\bullet} + \mu_b\theta\,\boldsymbol{I}, \tag{1.1}$$

where p is the thermodynamic pressure, $\boldsymbol{I}$ is the identity matrix, μ is the dynamic (or shear) viscosity, $\boldsymbol{D}^{\bullet} \equiv (\boldsymbol{\nabla u} + (\boldsymbol{\nabla u})^{\intercal})/2 - (\theta/3)\boldsymbol{I}$ is the deviatoric deformation tensor (where $^{\intercal}$ is the transpose), μ_b is the bulk viscosity, $\theta \equiv \boldsymbol{\nabla}\cdot\boldsymbol{u}$ is the dilatational rate and $\boldsymbol{u}$ is the velocity vector.

This form of the stress tensor represents a first-order correction (in $\boldsymbol{\nabla u}$) to the hydrostatic stress tensor ($-p\boldsymbol{I}$) experienced by a fluid element following its deformation at constant volume ($2\mu\boldsymbol{D}^{\bullet}$) and its compression/expansion ($\mu_b\theta\boldsymbol{I}$). The thermodynamic pressure is defined as the pressure obtained from the thermal equation of state $p = p(\rho, T)$ evaluated at density, ρ, and temperature, T. Both shear and bulk viscosities (as well as thermal conductivity, κ) ought to capture relaxation processes within the constituents of matter following a local change in its kinematics. Specifically, μ_b introduces a time lag between the mechanical pressure, p_m, which is imposed by the flow, and the one measured if all internal modes have equilibrated to the translational modes at the given (ρ, T) state

$$p_m = p - \mu_b\theta. \tag{1.2}$$

The ability to capture the relaxation of internal modes to equilibrium through a single parameter is questionable (see Meador, Miner & Townsend 1996, for example). Yet, such a simple approach is arguable if the kinetic energy of the fluid is changing over time scales much greater than those governing the repartition of internal modes, a condition referred to as the local thermodynamic equilibrium (LTE) condition (see Graves & Argrow 1999, and references therein). If satisfied, all transport properties (μ, κ and μ_b) have associated thermal equations of state, with no explicit time dependencies, consistently with the Newtonian-fluid model.

1.2. *Stokes' hypothesis and turbulent flows*

Numerous thermal equations of state for μ exist (e.g. power law, Sutherland's law) but are virtually non-existent for μ_b (see Cramer 2012). Thus, setting μ_b to zero, corresponding to the so-called Stokes' hypothesis, is often a modelling convenience, which is inconsequential in truly incompressible flows (where $\theta = 0$), rather than an actual statement on its thermal equation of state (Stokes' original intention, see Stokes 1845). Indeed, the few bulk-to-shear viscosity ratios inferred from sound absorptions in di- and tri-atomic gases all exceed unity (see Graves & Argrow 1999), sometimes by many orders of magnitudes (μ_b/μ values of the order of 10^4 in air with relative humidities of a few per cent are reported in Ash, Zuckerwar & Zheng 1991).

For turbulent flows, the significance of setting μ_b to zero on kinetic-energy transfers can be assessed by comparing the work (per unit time and volume) done by the thermodynamic pressure ($\boldsymbol{u} \cdot \boldsymbol{\nabla} p$) to that of the mechanical pressure ($\boldsymbol{u} \cdot \boldsymbol{\nabla} p_m$). For eddies with length scale, ℓ, and velocity scale, $\mathcal{U}$, in a fluid evolving about the thermodynamic state (ρ, T), this amounts to comparing the eddy Reynolds number, $Re_\ell \equiv \rho \mathcal{U} \ell / \mu$, with the product χM^2, where $\chi \equiv \mu_b/\mu$ is the bulk-to-shear viscosity ratio and $M \equiv \mathcal{U}/c$ is the eddy Mach number (c is the sound speed at the thermodynamic state). Stokes' hypothesis corresponds to the regime $Re_\ell \gg \chi M^2$. At dissipative scales, where $Re_\ell \sim 1$, Stokes' hypothesis translates to $\chi M^2 \ll 1$. For eddy Mach numbers of the order 10^{-1} (typical in shock-free turbulence), the solenoidal kinetic energy in the energy-rich inertial range (where $Re_\ell \gg 1$) is thus expected to remain undisrupted for χ values of up to 10^2, and setting $\mu_b = 0$ would be reasonable despite having $\mu_b > \mu$. In decaying homogeneous turbulence, Pan & Johnsen (2017) find no noticeable change in solenoidal kinetic energy (relative to when $\mu_b = 0$) for $M < 0.1$ and $\chi = 30$, confirming and greatly extending the results by Liao, Peng & Luo (2009) (given at $M \approx 0.5$, $\chi = 4/15$). In wall-bounded turbulence, Reynolds-stress profiles remain unchanged for both channel- ($M \approx 1.5$ and $\chi = 500$, Sciacovelli *et al.* 2017) and Couette-flow ($M \approx 3$ and $\chi = 10$, Szemberg O'Connor 2018) configurations. Similar findings are reported in turbulent mixing layers at $M \approx 0.5$ and $\chi \sim 10$ (Boukharfane 2018). For substances featuring large bulk-viscosity values ($\chi \gg 1$), the pressure–work scalings also suggest that a portion of the inertial range, if present, is likely to be directly affected by μ_b. If $\chi \sim 10^3$ and $M \sim 1$, Stokes' hypothesis would be valid for eddy Reynolds above a million. Pan & Johnsen (2017) give the first (and only) simulation of decaying homogeneous turbulence at $\chi = 1000$. The solenoidal kinetic energy at high wavenumbers (low Re_ℓ) is eroded relative to the $\mu_b = 0$ case. Such erosion is rooted in the rapid dissipation of the dilatational kinetic energy by the bulk viscosity, which is irreversibly transferred to the internal energy (via $\mu_b \theta^2$), thereby decreasing the overall available kinetic energy to transfer from the large (set by the initial condition) to the small scales. Whilst promising, the results are based on a single simulation at low Reynolds number that did not feature an inertial range, making the distinction between viscous dissipation and bulk-viscosity effects difficult (see later). Moreover, the nature of the thermodynamic pressure fluctuations at small scales was not considered but will be shown here to present a more complex picture than that associated with the damping or suppression of acoustic waves at small scales.

Systematic experimental and numerical studies of the effect of bulk viscosity on compressible turbulence are therefore desperately needed. Direct simulations of high Reynolds flows of high-χ fluids are χ times more expensive to integrate in time than if $\mu_b = 0$ (owing to the viscous stability constraint and assuming the spatial resolution to be the same). For carbon dioxide flows, for which $\chi \sim 10^3$, this translates to studies

thousands of times more expensive than if $\mu_b = 0$. The prohibitive computational cost is, and will continue to be, a major obstacle. Thus, a more pragmatic approach capable of providing a definite answer to the question 'can high-χ fluids directly interfere with the inertial range?' is needed. The present work sets to provide scaling arguments to assess the importance of μ_b to the turbulence kinetic energy redistribution, which are based on exact solutions to the linearised Navier–Stokes equations (§ 2). Illustrations in two-dimensional turbulence, for which the computational cost is more amenable, are provided together with arguments about the importance of the results to (more realistic) three-dimensional flows (§ 3).

2. Eigenmodes

The motion of a Newtonian fluid satisfying the LTE assumption (see § 1.1) is considered throughout the paper. The time (t) evolution of the density, velocity and total specific energy (e_t) fields follow from the application of the mass-conservation, momentum-balance and energy-conversion principles assuming Fourier's law of thermal conduction (giving the compressible Navier–Stokes equations)

$$\frac{\partial}{\partial t}\begin{bmatrix}\rho\\ \rho\boldsymbol{u}\\ \rho e_t\end{bmatrix}+\boldsymbol{\nabla}\cdot\begin{bmatrix}\rho\boldsymbol{u}\\ \rho\boldsymbol{u}\otimes\boldsymbol{u}+p_m\boldsymbol{I}-2\mu\boldsymbol{D}^{\bullet}\\ (\rho e_t+p_m-2\mu\boldsymbol{D}^{\bullet})\,\boldsymbol{u}-\kappa\boldsymbol{\nabla}T\end{bmatrix}=\boldsymbol{0}, \tag{2.1}$$

where $e_t \equiv e + \boldsymbol{u}\cdot\boldsymbol{u}/2$ and e is the specific internal energy. The fluid is assumed to be thermally and calorically perfect, i.e. $p = \rho RT$ and $\mathrm{d}e = c_v \mathrm{d}T$, where 'd' is the differential operator, R is the gas constant and c_v is the (assumed constant) isochoric specific heat, which relates to the isobaric specific heat (c_p) according to Mayer's relation, $R = c_p - c_v = c_v(\gamma - 1)$, where $\gamma \equiv c_p/c_v$ is the specific heat ratio.

All transport coefficients (i.e. μ, μ_b, κ) are assumed constant and uniform. This choice is motivated by the associated simplicity but also the will to isolate effects relating to compressibility (rather than include those associated with the gradients of the transport coefficients, see Lele 1994). The intention is to highlight the effects of μ_b on the flow properties rather than achieve a high degree of realism (i.e. by matching as many properties of an existing fluid). Instead, the range of μ_b/μ values is kept consistent with those found in the literature.

Note that the factor '1/3' used to extract the deviatoric part of the deformation tensor ($\boldsymbol{D}^{\bullet}$, see below (1.1)) comes with the underlying assumption that the fluid evolves in three-dimensional space. Although the present work concentrates on one- and two-dimensional analyses, these are still carried out with the one-third factor. This choice should therefore be interpreted as relating to three-dimensional flows featuring (artificially imposed) uniform directions instead. The orthogonal unit vectors $\boldsymbol{e}_x, \boldsymbol{e}_y, \boldsymbol{e}_z$ span the three-dimensional space, and $\mathscr{O}$ is the origin of a Cartesian coordinate system with coordinates x, y, z in the $\boldsymbol{e}_x$, $\boldsymbol{e}_y$ and $\boldsymbol{e}_z$ directions, respectively.

The response of the governing equations (2.1) to a small perturbation of an otherwise uniform flow is now considered to gain valuable insights into the way μ_b interferes with the flow unsteadiness (and turbulence in particular). For simplicity, the flow is assumed aligned with $\boldsymbol{e}_x$ (i.e. $v = w = 0$) and independent of y and z at all times (i.e. $\rho = \rho(x, t)$, $u = u(x, t)$, $p = p(x, t)$). Let ρ_0, u_0 and p_0 define constant and uniform (in all directions) density, velocity and pressure fields. Those fields are referred to as base flow thereafter. Let ρ_1, u_1, p_1 define perturbations of the

base flow

$$\begin{cases} \rho = \rho_0 + \varepsilon\, \rho_1, \\ u = u_0 + \varepsilon\, u_1, \\ p = p_0 + \varepsilon\, p_1, \end{cases} \tag{2.2}$$

where ε is a non-dimensional control parameter (chosen such that $\varepsilon \ll 1$). Injecting (2.2) in (2.1) and matching first-order terms in ε gives

$$\frac{\partial \boldsymbol{\mu}_1}{\partial t} + \begin{bmatrix} u_0 & \rho_0 & 0 \\ 0 & u_0 & \dfrac{1}{\rho_0} \\ 0 & \gamma p_0 & u_0 \end{bmatrix} \frac{\partial \boldsymbol{\mu}_1}{\partial x} + \begin{bmatrix} 0 & 0 & 0 \\ 0 & -\dfrac{1}{\rho_0}\left(\dfrac{4}{3}\mu + \mu_b\right) & 0 \\ \dfrac{\mu\gamma p_0}{\rho_0^2 Pr} & 0 & -\dfrac{\mu\gamma}{\rho_0 Pr} \end{bmatrix} \frac{\partial^2 \boldsymbol{\mu}_1}{\partial x^2} = \boldsymbol{0}, \tag{2.3}$$

where $\boldsymbol{\mu}_1 \equiv [\rho_1, u_1, p_1]^\intercal$ is the vector of perturbed primitive variables, and $Pr \equiv \mu c_p/\kappa$ is the Prandtl number.

Plane-wave solutions to (2.3) are sought

$$\boldsymbol{\mu}_1 = \begin{bmatrix} \rho_0 & 0 & 0 \\ 0 & c_0 & 0 \\ 0 & 0 & p_0 \end{bmatrix} \tilde{\boldsymbol{\mu}} \exp[\mathrm{i}(\omega t - kx)], \quad \text{with } k \in \mathbb{C},\ \omega \in \mathbb{R}_{>0}, \tag{2.4}$$

where $\tilde{\boldsymbol{\mu}} \equiv [\tilde{\rho}, \tilde{u}, \tilde{p}]^\intercal$ is a vector of dimensionless amplitudes for the primitive variables, $c_0 = \sqrt{\gamma p_0/\rho_0}$ is the (base flow) sound speed, k is the (complex) wavenumber and ω is the (real, strictly positive) angular frequency (and $\mathrm{i}^2 = -1$). Injecting (2.4) into (2.3) gives

$$\boldsymbol{L}\,\tilde{\boldsymbol{\mu}} = \boldsymbol{0}, \tag{2.5}$$

where

$$\boldsymbol{L} \equiv \boldsymbol{A} - \lambda \boldsymbol{I}, \quad \boldsymbol{A} \equiv \begin{bmatrix} 0 & -\zeta & 0 \\ 0 & -\mathrm{i}\dfrac{\zeta^2}{\tilde{Re}}\left(\dfrac{4}{3} + \chi\right) & -\dfrac{\zeta}{\gamma} \\ \mathrm{i}\dfrac{\gamma\zeta^2}{\tilde{Re} Pr} & -\gamma\zeta & -\mathrm{i}\dfrac{\gamma\zeta^2}{\tilde{Re} Pr} \end{bmatrix}, \quad \lambda \equiv \zeta \mathscr{M} - 1, \tag{2.6}$$

and $\zeta \equiv kc_0/\omega$, $\mathscr{M} \equiv u_0/c_0$, $\tilde{Re} \equiv \rho_0 c_0^2/(\mu\omega)$, $\chi \equiv \mu_b/\mu$. In what follows, $\tilde{Re}$ is referred to as the acoustic Reynolds number.

For given flow conditions ($\mathscr{M}$, $\tilde{Re}$) and gas properties (γ, χ, Pr), the determinant of $\boldsymbol{L}$

$$\det(\boldsymbol{L}) = \lambda(\zeta^2 - \lambda^2) - \frac{\mathrm{i}\zeta^2}{\tilde{Re}}\left[\lambda^2\left(\frac{4}{3} + \chi + \frac{\gamma}{Pr}\right) - \frac{\zeta^2}{Pr}\right] + \frac{\zeta^4 \lambda}{\tilde{Re}^2}\frac{\gamma}{Pr}\left(\frac{4}{3} + \chi\right), \tag{2.7}$$

defines a polynomial (up to fifth order) in ζ. Non-trivial solutions to (2.5) exist if (and only if) $\det(\boldsymbol{L}) = 0$. The roots (ζ) of the polynomial provide (up to five) dispersion relations (i.e. $\omega(k) = 0$). Each dispersion relation gives one eigenvalue $\lambda = \zeta\mathscr{M} - 1$ and an associated eigenvector $\tilde{\boldsymbol{\mu}}$. The (ζ, $\tilde{\boldsymbol{\mu}}$) pairs are referred to as the eigenmodes. Before commenting on the effect of χ on the eigenmodes, particular regimes on the Re(ζ)–Im(ζ) plane are first extracted.

2.1. *Asymptotic regimes*

2.1.1. *Euler limit ($\tilde{Re} \to \infty$)*

In the limit of infinite acoustic Reynolds number (i.e. $\mu\omega \to 0$), $\det(\boldsymbol{L}) = 0$ simplifies to $\lambda(\zeta^2 - \lambda^2) = 0$, giving $\lambda = 0$ and $\lambda = \pm\zeta$, or equivalently $\zeta = 1/\mathscr{M}$ and $\zeta = 1/(\mathscr{M} \pm 1)$. The eigenmodes are

$$\sigma = \left\{ (\zeta, \tilde{\boldsymbol{\mu}}) \in \mathbb{R} \times \mathbb{R}^3 : \zeta = \frac{1}{\mathscr{M}}, \tilde{\boldsymbol{\mu}} = \phi \begin{bmatrix} 1 \\ 0 \\ 0 \end{bmatrix} \right\}, \tag{2.8a}$$

$$a^{\pm} = \left\{ (\zeta, \tilde{\boldsymbol{\mu}}) \in \mathbb{R} \times \mathbb{R}^3 : \zeta = \frac{1}{\mathscr{M}_{\pm}}, \tilde{\boldsymbol{\mu}} = \phi \begin{bmatrix} 1 \\ \pm 1 \\ \gamma \end{bmatrix} \right\}, \tag{2.8b}$$

where $\phi \in \mathbb{R}_{\neq 0}$ is a non-zero parameter (which in practice is absorbed by the smallness parameter, ε) and $\mathscr{M}_{\pm} \equiv \mathscr{M} \pm 1$. These eigenmodes are the so-called Kovásznay eigenmodes (see Kovásznay 1953, for details). They correspond to entropy waves (σ) characterised by pure density fluctuations propagating at the flow speed (i.e. with phase speed u_0), and two acoustic waves, one propagating downstream (a^+, with phase speed $u_0 + c_0$) and one propagating upstream (a^-, with phase speed $u_0 - c_0$). These eigenmodes form a basis that is extensively discussed in Alferez & Touber (2017) in the context of arbitrary fluids. In this work, σ, a^+ and a^- act as useful markers in the Re(ζ)–Im(ζ) plane since they all lie on the real axis (i.e. these modes have no spatial damping).

2.1.2. *Landau regime ($\tilde{Re} \gg 1$)*

In the limit of large but finite acoustic Reynolds number (i.e. $\mu\omega \ll \gamma p_0$), the wavenumber (k, or its dimensionless form ζ) is complex, reflecting the damping effect of transport coefficients on the Euler modes. Analytical expressions for the departure from the Euler modes in the Re(ζ)–Im(ζ) plane are obtained by seeking a solution in the form $\zeta = a + \mathrm{i}b/\tilde{Re}$ where a assumes the ζ value obtained from the Euler modes. Injecting such form in (2.7), expanding in powers of $1/\tilde{Re}$, and cancelling terms up to first order provide expressions for b. A similar approach is used to find the eigenvectors (i.e. seeking a solution in the form $\tilde{\boldsymbol{\mu}} = \tilde{\boldsymbol{\mu}}_0 + (\boldsymbol{a} + \mathrm{i}\boldsymbol{b})/\tilde{Re}$ up to first order in $1/\tilde{Re}$, where $\tilde{\boldsymbol{\mu}}_0$ is the corresponding eigenvector in the Euler limit). The resulting eigenmodes are

$$\mathscr{S} = \left\{ (\zeta, \tilde{\boldsymbol{\mu}}) \in \mathbb{C} \times \mathbb{C}^3 : \zeta = \frac{1}{\mathscr{M}} - \frac{\mathrm{i}}{\tilde{Re}Pr\mathscr{M}^3}, \tilde{\boldsymbol{\mu}} = \phi \begin{bmatrix} 1 \\ \mathrm{i}/[\tilde{Re}Pr\mathscr{M}] \\ 0 \end{bmatrix} \right\}, \tag{2.9a}$$

$$\mathscr{L}^{\pm} = \left\{ (\zeta, \tilde{\boldsymbol{\mu}}) \in \mathbb{C} \times \mathbb{C}^3 : \zeta = \frac{1}{\mathscr{M}_{\pm}} - \frac{\mathrm{i}\delta^+}{2\tilde{Re}\mathscr{M}_{\pm}^3}, \tilde{\boldsymbol{\mu}} = \phi \begin{bmatrix} 1 \mp \dfrac{\mathrm{i}(\gamma - 1)}{\tilde{Re}Pr\mathscr{M}_{\pm}} \\ \pm 1 + \dfrac{\mathrm{i}\delta^-}{2\tilde{Re}\mathscr{M}_{\pm}} \\ \gamma \end{bmatrix} \right\}, \tag{2.9b}$$

where $\phi \in \mathbb{C}_{\neq 0}$ and $\delta^{\pm} \equiv 4/3 + \chi \pm (\gamma - 1)/Pr$ (note that $\tilde{\boldsymbol{\mu}}$ can be arbitrarily stretched and rotated on the complex plane by ϕ, it is set here to align with $\tilde{p}$ in (2.8*b*) for $\phi = 1$). The damping coefficient $\mathrm{Im}(\zeta) = -\delta^{+}/(2\tilde{Re}\mathscr{M}_{\pm}^{3})$ for the acoustic modes $\mathscr{L}^{\pm}$ (with δ^{+} the non-dimensional Kirchoff diffusivity), corresponds to the well-known acoustic damping found by Landau & Lifshitz (1987) (equation (79.6) on page 301 of the 2nd edition), which is corrected here to account for a non-zero base-flow velocity (i.e. when $u_0 \neq 0$). The above result also offers a more complete picture since the damping is clearly identified as a first-order correction (in $1/\tilde{Re}$) to Kovásznay eigenmode basis (including that of the entropy mode $\mathscr{S}$), with explicit expressions for the coordinates (ρ, u, p) of each eigenmode in the primitive-variable basis. This will be useful when discussing the effect of μ_b on turbulence.

2.1.3. *Stokes regime ($\tilde{Re} \ll 1$)*

In the limit of small acoustic Reynolds number (i.e. $\mu\omega \gg \gamma p_0$), the wavenumber (k, or its dimensionless form ζ) is again complex but is anticipated to align with the (stable) diagonal of the $\mathrm{Re}(\zeta)$–$\mathrm{Im}(\zeta)$ plane. This reflects the tendency towards a diffusion-dominated flow, and in particular the celebrated 'second problem of Stokes' (i.e. oscillating plate), which has solutions in the form $\sin(\omega t - Kx)\exp(-Kx)$ with $Kc_0/\omega = (\tilde{Re}/2)^{1/2}$. Thus, one expects that in the limit of small acoustic Reynolds number, $\zeta = \eta\Gamma\exp(-\mathrm{i}\pi/4)$ where $\eta \in \mathbb{R}_{\neq 0}$ and $\Gamma \equiv \tilde{Re}^{1/2}$. Injecting such form in (2.7) and expanding in powers of Γ gives

$$\det(\boldsymbol{L}) \underset{\Gamma\to 0}{=} \left\{A + \frac{(B-A)\eta\mathscr{M}}{\sqrt{2}}\Gamma + O(\Gamma^2)\right\} - \mathrm{i}\left\{\frac{(B-A)\eta\mathscr{M}}{\sqrt{2}}\Gamma + O(\Gamma^2)\right\}, \quad (2.10)$$

where $A \equiv \alpha\beta\eta^4 - (\alpha+\beta)\eta^2 + 1$, $B \equiv (\alpha+\beta)\eta^2 - 2$, with $\alpha \equiv 4/3 + \chi$, $\beta \equiv \gamma/Pr$ (note that A and B are real). A necessary (and sufficient) condition for non-trivial solutions to (2.5) to exist (in the required form and up to first order in Γ) is $A = 0$ and $B\mathscr{M} = 0$. Setting $A = 0$ gives $\eta^2 = 1/\alpha$ or $\eta^2 = 1/\beta$. If $\mathscr{M} \neq 0$ the second statement ($B\mathscr{M} = 0$) requires that $\eta^2 = 2/(\alpha+\beta)$, which is compatible with the condition $A = 0$ if $\alpha = \beta$. If $\mathscr{M} = 0$ ($u_0 = 0$), the condition $A = 0$ suffices. In practice, setting either $\mathscr{M} = 0$ or $\alpha = \beta$ may be too restrictive. Instead, let $u_\phi \equiv \omega/\mathrm{Re}(k)$ denote the phase speed and note that $\eta\mathscr{M}\Gamma/\sqrt{2} = u_0/u_\phi$. Thus, the $O(\Gamma)$ terms in (2.10) may be neglected when considering large phase speeds (compared to that of the base flow, i.e. $u_\phi \gg u_0$, independently of how large u_0 is), and setting $A = 0$ becomes a sufficient condition for non-trivial solutions to exist. The eigenmodes corresponding to roots $\eta = \pm 1/\sqrt{\alpha}$ and $\eta = \pm 1/\sqrt{\beta}$ (in the limit of $u_0/u_\phi \to 0$) are

$$\mathscr{U}^{\pm} = \left\{(\zeta, \tilde{\boldsymbol{\mu}}) \in \mathbb{C}\times\mathbb{C}^3 : \zeta = \pm\sqrt{\frac{\tilde{Re}}{2\alpha}}(1-\mathrm{i}),\ \tilde{\boldsymbol{\mu}} = \phi\begin{bmatrix}0\\1\\0\end{bmatrix}\right\}, \quad (2.11a)$$

$$\mathscr{P}^{\pm} = \left\{(\zeta, \tilde{\boldsymbol{\mu}}) \in \mathbb{C}\times\mathbb{C}^3 : \zeta = \pm\sqrt{\frac{\tilde{Re}}{2\beta}}(1-\mathrm{i}),\ \tilde{\boldsymbol{\mu}} = \phi\begin{bmatrix}0\\0\\1\end{bmatrix}\right\}, \quad (2.11b)$$

where $\phi \in \mathbb{C}_{\neq 0}$. They correspond to the diffusion of velocity ($\mathscr{U}^{\pm}$) and pressure ($\mathscr{P}^{\pm}$) fluctuations in (+) and against (−) the flow direction ('ploughing' space at arbitrarily fast phase speeds). For a given shear viscosity μ, these eigenmodes become increasingly relevant to small-wavelength waves (high-frequency 'sound').

Note the scaling in $\tilde{Re}^{1/2}$, implying that higher frequencies are less damped than lower frequencies. This is to contrast with the Landau regime, where the opposite is true.

Finally, if $\mathscr{M} \neq 0$, injecting $\zeta = (1 + \mathrm{i}b\tilde{Re})/\mathscr{M}$ in (2.7) gives

$$\mathscr{M}^4 \det(\boldsymbol{L}) = \{4b(X^2-1)Z - 2YX^2\mathscr{M}^2\} + \mathrm{i}\left\{X[X^2(\mathscr{M}^2 - Y) + Y]\mathscr{M}^2 + [(1-X^2)^2 - 4X^2]\frac{Z}{\tilde{Re}}\right\}, \quad (2.12)$$

where $X \equiv b\tilde{Re}$, $Y \equiv 1 + b(\alpha + \beta)$ and $Z \equiv \alpha\beta b + 1/Pr$. Setting $Z = 0$ (i.e. $b = -1/(\alpha\beta Pr) = -1/(\gamma\alpha)$) then gives

$$\det(\boldsymbol{L}) \underset{\tilde{Re}\to 0}{=} \{O(\tilde{Re}^2)\} + \mathrm{i}\{O(\tilde{Re})\}. \quad (2.13)$$

Therefore, in the limit of vanishing acoustic Reynolds number ($\tilde{Re} \to 0$) and in the presence of a base flow ($u_0 \neq 0$), the following eigenmode is also considered

$$\mathscr{N} = \left\{(\zeta, \tilde{\boldsymbol{\mu}}) \in \mathbb{C} \times \mathbb{R}^3 : \zeta = \frac{1}{\mathscr{M}} - \frac{\mathrm{i}\tilde{Re}}{\gamma\alpha\mathscr{M}}, \tilde{\boldsymbol{\mu}} = \phi \begin{bmatrix} 1 \\ 0 \\ 1 \end{bmatrix}\right\}. \quad (2.14)$$

Whilst reminiscent of the Euler entropy mode (σ), mode $\mathscr{N}$ has equal coordinates in ρ and p, i.e. $|p - p_0|/p_0 \sim |\rho - \rho_0|/\rho_0 \sim \varepsilon\phi$. Noting that $p(\rho_0 + \varepsilon\rho_0, T_0) - p(\rho_0, T_0) \sim \varepsilon\rho_0(\partial p/\partial\rho)_{T=T_0} = \varepsilon\rho_0 a_0^2 = \varepsilon p_0$ (where a_0 is Newton's isothermal speed of sound), mode $\mathscr{N}$ corresponds to the transport by the base flow of isothermally compressed (or expanded) fluid particles (relative to the base state). It is referred here as Newton mode in reference to the isothermal compression of fluid particles. The Newton mode ($\mathscr{N}$) will be shown to smoothly reconnect to the Euler entropy mode (σ) when the bulk viscosity is large, and to play a primary role in promoting the solenoidal kinetic energy of small-scale turbulence.

2.1.4. *Graphical summary of the asymptotic regimes*

Figure 1 provides a qualitative summary of the asymptotic limits discussed in the previous paragraphs. The vertical axis represents the damping factor $\mathrm{Im}(\zeta)$. The horizontal axis represents the phase Mach number, $\mathscr{M}_\phi = 1/\mathrm{Re}(\zeta)$. In the limit of infinite acoustic Reynolds number, the dispersion relation converges to the Euler modes ($a^\pm$, σ). These limits are reached via the Landau modes ($\mathscr{S}$, $\mathscr{L}^\pm$) presented in § 2.1.2. In the limit of vanishing acoustic Reynolds number, the dispersion relation converges to the Newton ($\mathscr{N}$) and Stokes diffusion ($\mathscr{U}^\pm$, $\mathscr{P}^\pm$) modes described in § 2.1.3. Both limits ($\tilde{Re} \to \infty$ and $\tilde{Re} \to 0$) assume undamped solutions and thus lie on the real axis. In the Stokes diffusion case, such limit takes the form of infinite phase speeds (i.e. $\mathscr{M}_\phi \to \pm\infty$ when $\tilde{Re} \to 0$ along the $\mathscr{U}^\pm$ and $\mathscr{P}^\pm$ branches).

On the $\mathscr{M}_\phi$–$\mathrm{Im}(\zeta)$ plane, both the Landau ($\mathscr{S}$, $\mathscr{L}^\pm$) and Newton ($\mathscr{N}$) branches connect to the $\mathscr{M}_\phi$ axis following a vertical tangent. However, note the directional difference for the $\mathscr{N}$ branch, which departs from σ (contrary to the $\mathscr{S}$ mode). The Stokes diffusion modes ($\mathscr{U}^\pm$, $\mathscr{P}^\pm$) follow a path with a $-1/\mathscr{M}_\phi$ scaling. For a given fluid and base flow, the acoustic Reynolds number ($\tilde{Re}$) plays the role of a coordinate along each branch (corresponding to changing the forcing frequency). With this in mind, note from (2.11) that despite being superimposed, the same point on the $\mathscr{U}$

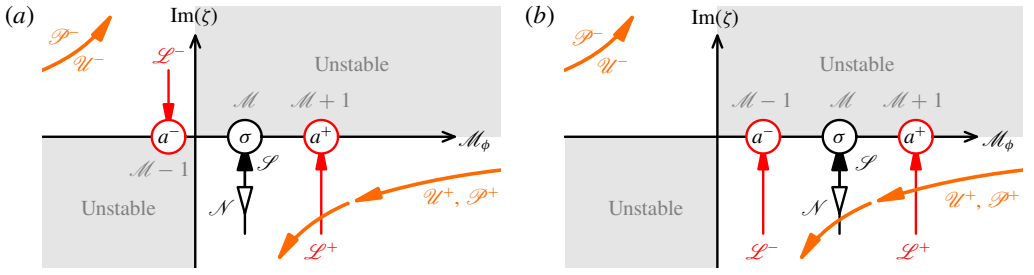

FIGURE 1. (Colour online) Graphical summary of the asymptotic limits of $\det(\boldsymbol{L}) = 0$ for $\mathscr{M} < 1$ (*a*) and $\mathscr{M} > 1$ (*b*) representing the damping factor $\mathrm{Im}(\zeta)$ as a function of the phase Mach number $\mathscr{M}_\phi = 1/\mathrm{Re}(\zeta)$. Arrows point in the direction of increasing $\tilde{Re}$ values. On the real axis ($\mathscr{M}_\phi$) lie the Euler solutions ($a^\pm$, σ), which are reached by the Landau branches ($\mathscr{L}^\pm$, $\mathscr{S}$) when $\tilde{Re} \to \infty$. In contrast, the Newton branch ($\mathscr{N}$) and Stokes diffusion branches ($\mathscr{U}^\pm$, $\mathscr{P}^\pm$) depart from the real axis as $\tilde{Re}$ is increased (vertically down for $\mathscr{N}$ and according to $-1/\mathscr{M}_\phi$ for $\mathscr{U}$ and $\mathscr{P}$). The eight branches shown here act as guidelines to actual solutions to $\det(\boldsymbol{L}) = 0$, which continuously transition from one Stokes branch to one Landau branch, as shown in figure 2.

and $\mathscr{P}$ branches correspond to different $\tilde{Re}$ coordinates (due to the different stretching factors, $1/\sqrt{\alpha}$ versus $1/\sqrt{\beta}$).

Owing to the choice of plane-wave definition (see (2.4)), stable modes have a negative damping factor if propagating in the $x > 0$ direction, and a positive damping factor if propagating in the $x < 0$ direction. All asymptotic regimes give linearly stable modes. For supersonic base flows ($\mathscr{M} > 1$), the $\mathscr{L}^-$ branch moves from the ($\mathscr{M}_\phi < 0$, $\mathrm{Im}(\zeta) > 0$) quadrant to the ($\mathscr{M}_\phi > 0$, $\mathrm{Im}(\zeta) < 0$) quadrant. This is due to the $\mathscr{M}_-$ term in (2.9*b*). Unlike for Euler flows, viscous and thermally conductive supersonic flows still sustain two modes ($\mathscr{U}^-$ and $\mathscr{P}^-$) travelling upstream of the source point, which are less and less damped as the forcing frequency is increased.

2.2. *Continuous 'acoustic' and 'entropy' paths*

2.2.1. ***L**-matrix spectrum*

The asymptotic branches discussed in the previous paragraphs are now combined with numerical solutions of $\det(\boldsymbol{L}) = 0$ to extract and interpret particular paths in the phase-speed ($\mathscr{M}_\phi$) and damping-factor ($\mathrm{Im}(\zeta)$) plane. All numerical solutions presented here consider carbon dioxide in atmospheric conditions (i.e. $\gamma = 1.29$, $Pr = 0.7$) flowing at $\mathscr{M} = 0.5$. However, the asymptotic solutions given above can readily be used to anticipate the effect of changing the specific heat ratio, the Prandtl number and the base-flow speed on the results presented here.

Figure 2 gives the dispersion relations (i.e. roots of (2.7), obtained numerically) for four different μ_b/μ ratios ($\chi \in \{0, 10, 10^2, 10^3\}$) over a range of acoustic Reynolds numbers ($\tilde{Re} \in [10^{-3}, 10^5]$). The damping factor, $\mathrm{Im}(\zeta)$, is plotted against the phase Mach number, $\mathscr{M}_\phi = 1/\mathrm{Re}(\zeta)$. Since $\mathscr{M}$, μ and κ are all chosen to be non-zero, (2.7) is a fifth-order polynomial, giving five (distinct) roots. Each root describes one branch in figure 2 when varying $\tilde{Re}$ (keeping everything else constant), giving a total of five branches. In agreement with the asymptotic analyses, all branches from the numerical solutions are linearly stable.

The branches are made thicker when $\tilde{Re} > 10$ to identify the parts of the branches corresponding to higher acoustic Reynolds numbers. The low- and high-$\tilde{Re}$ ends of

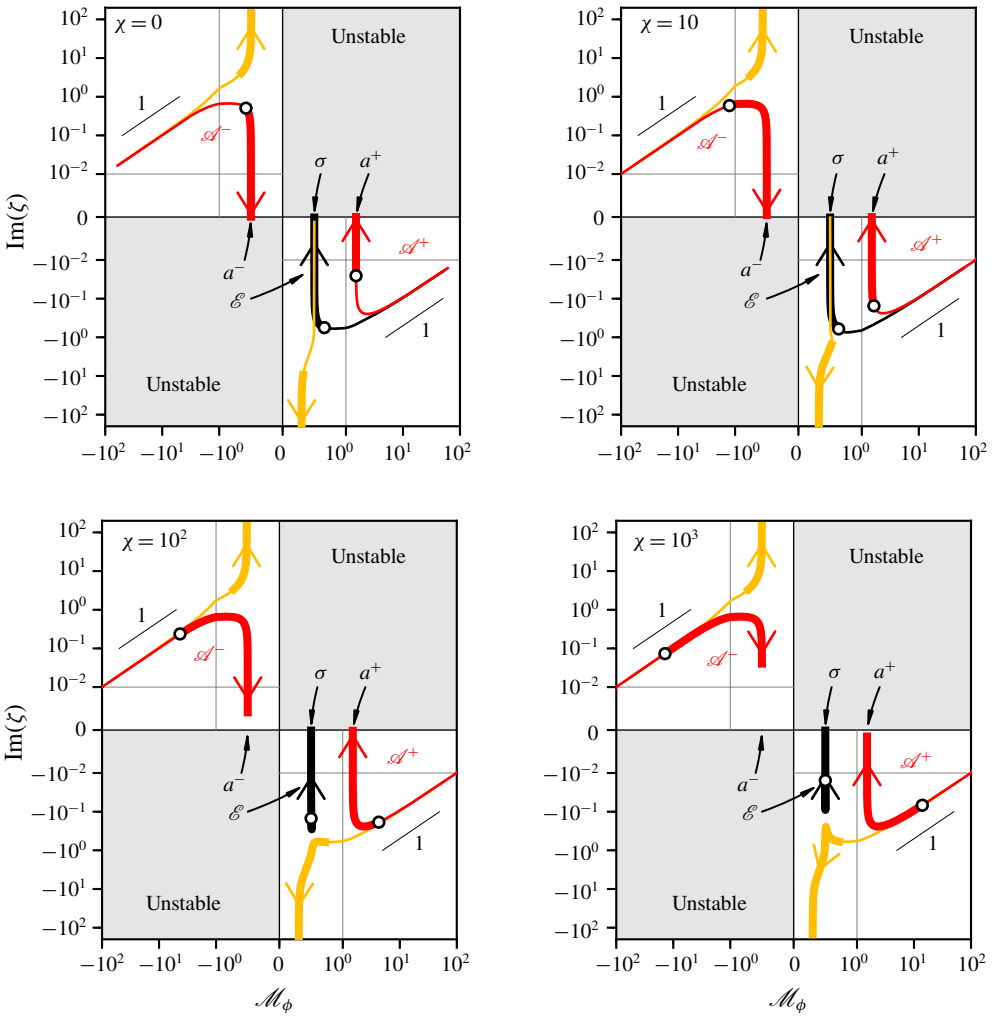

FIGURE 2. (Colour online) Damping factor, $\mathrm{Im}(\zeta)$, and phase Mach number, $\mathscr{M}_\phi$, of the eigenmodes obtained from numerical solutions of $\det(\boldsymbol{L}) = 0$ for a range of acoustic Reynolds numbers ($\tilde{Re} \in [10^{-3}, 10^{5}]$) and bulk- to shear-viscosity ratios ($\chi \in \{0, 10, 10^2, 10^3\}$, indicated inside each panel). The base flow is set to $\mathscr{M} = 0.5$, together with $\gamma = 1.29$ and $Pr = 0.7$. The acoustic ($\mathscr{A}^{\pm}$) and entropy ($\mathscr{E}$) paths are identified in red and black, respectively (branches not taking part in these paths are shown in orange). The Euler modes (σ, $a^{\pm}$) are indicated along the real axis for reference. A marker (white circle) is shown on the acoustic and entropy paths to indicate the $\tilde{Re} = 10$ coordinates, where the line is made thicker on the side corresponding to $\tilde{Re} > 10$. Arrows on each path also give the direction of increasing $\tilde{Re}$ values. A mixture of log–log, linear and semi-log scales is used. The log–log and linear quadrants are marked with thin grey lines.

each branch are constrained by two of the asymptotic regimes discussed in figure 1. Solutions to $\det(\boldsymbol{L}) = 0$ thus form continuous paths connecting the Stokes and Landau regimes. In reference to the Euler mode they reach (when $\tilde{Re} \to \infty$), three particular paths in the $\mathscr{M}_\phi$–$\mathrm{Im}(\zeta)$ plane are considered.

(i) Two continuous acoustic paths ($\mathscr{A}^{\pm}$): the Landau acoustic mode ($\mathscr{L}$) connects to one of the Stokes diffusion mode ($\mathscr{U}$ or $\mathscr{P}$) and forms an acoustic path ($\mathscr{A}$), shown in red in figure 2. The Stokes regime in the (signed) log–log portions of the plot is characterised by a unitary slope. In the cases shown here, $\mathscr{P}$ is found to connect to $\mathscr{L}$ for $\chi = 0$, and $\mathscr{U}$ to $\mathscr{L}$ for $\chi \in \{10, 10^2, 10^3\}$. Remarkably, the shape of the acoustic path is not sensitive to the choice of χ (for given γ, Pr and $\mathscr{M}$ values). Rather, χ plays the role of a stretching factor on the $\tilde{Re}$ coordinate along the acoustic path (this is visible from the δ^+ and $1/\sqrt{\alpha}$ factors in (2.9*b*) and (2.11*a*)). This is illustrated by the displacement of the white circle (placed at $\tilde{Re} = 10$) along the $\mathscr{A}^{\pm}$ paths from one χ case to another in figure 2 (the marker recedes into the Stokes regime as χ is increased).

(ii) One continuous entropy path ($\mathscr{E}$): the Landau entropy branch ($\mathscr{S}$) either connects to one of the Stokes diffusion branches ($\mathscr{U}^+$ for $\chi = 0$, $\mathscr{P}^+$ for $\chi = 10$) or the Newton branch ($\mathscr{N}$ for $\chi \in \{10^2, 10^3\}$). The resulting continuous entropy paths are shown in black in figure 2. The entropy path for the high-χ cases shown here therefore describes a closed loop in $\mathscr{M}_\phi$–Im(ζ) space (figure 2*c*,*d*).

The (two) remaining branches, shown in orange in figure 2, diverge as $\tilde{Re} \to \infty$. These modes vanish (they are infinitely damped) in the Euler limit. If the base flow is supersonic ($\mathscr{M} > 1$, not shown here), then the remaining (orange) branch on the $\mathscr{M}_\phi > 0$ side of figure 2 (the one not connected to either σ or a^+) is the branch connecting to the upstream-propagating acoustic mode (a^-, which will now be on the $\mathscr{M}_\phi > 0$ side), whilst the two upstream-going Stokes diffusion branches ($\mathscr{U}^-$ and $\mathscr{P}^-$) are the ones diverging in the Euler limit and not forming a part of the acoustic or entropy paths.

The acoustic and entropy paths are parametrised by the acoustic Reynolds number. Figure 3 gives the evolution of the magnitude of the real and imaginary parts of the wavenumber ζ along the $\mathscr{A}^+$ and $\mathscr{E}$ paths (for all four values of χ) obtained from numerical solutions to $\det(\boldsymbol{L}) = 0$. Superimposed are the different asymptotic solutions described in §§ 2.1.2 and 2.1.3. The asymptotic solutions are in remarkable agreement with the numerical results over the Stokes and Landau regimes. The transition between the two regimes is limited to about one decade in $\tilde{Re}$. In all cases, the transition corresponds to a maximum in the damping factor. For the acoustic path, χ operates a shift in $\tilde{Re}$ of the curve without modifying its overall shape. This confirms the above observation that the acoustic path is unchanged (for given γ, Pr and $\mathscr{M}$ values) and that χ provides an alternative way of exploring this path at fixed $\tilde{Re}$. In contrast, the entropy path cannot be explored via χ alone: first, because the Landau regime ($\mathscr{S}$) is independent of χ; second, because the path itself changes with χ in the Stokes regime either because a different branch is selected or because the intercept with the Landau regime shifts (see figure 3*d*) owing to the fixed position of the Landau branch $\mathscr{S}$. Note that this last case implies that the maximum damping on the primitive variables associated with the entropy path will reduce as χ is increased, a rather counterintuitive effect of μ_b (i.e. more bulk viscosity leads to less damping).

2.2.2. *Eigenvectors*

The relative amplitudes of the primitive variables (ρ, u, p) along the $\mathscr{A}^+$ and $\mathscr{E}$ paths on the surface of one eighth of the unit sphere are explored in figure 4 (see caption for details), enabling the visualisation of the smooth transition from one of the Stokes limit ((2.9) and (2.11)) to the Euler limit (2.8). For the acoustic path, starting from either a pure fluctuation in p ($\mathscr{P}^+$) or u ($\mathscr{U}^+$), most of the displacement

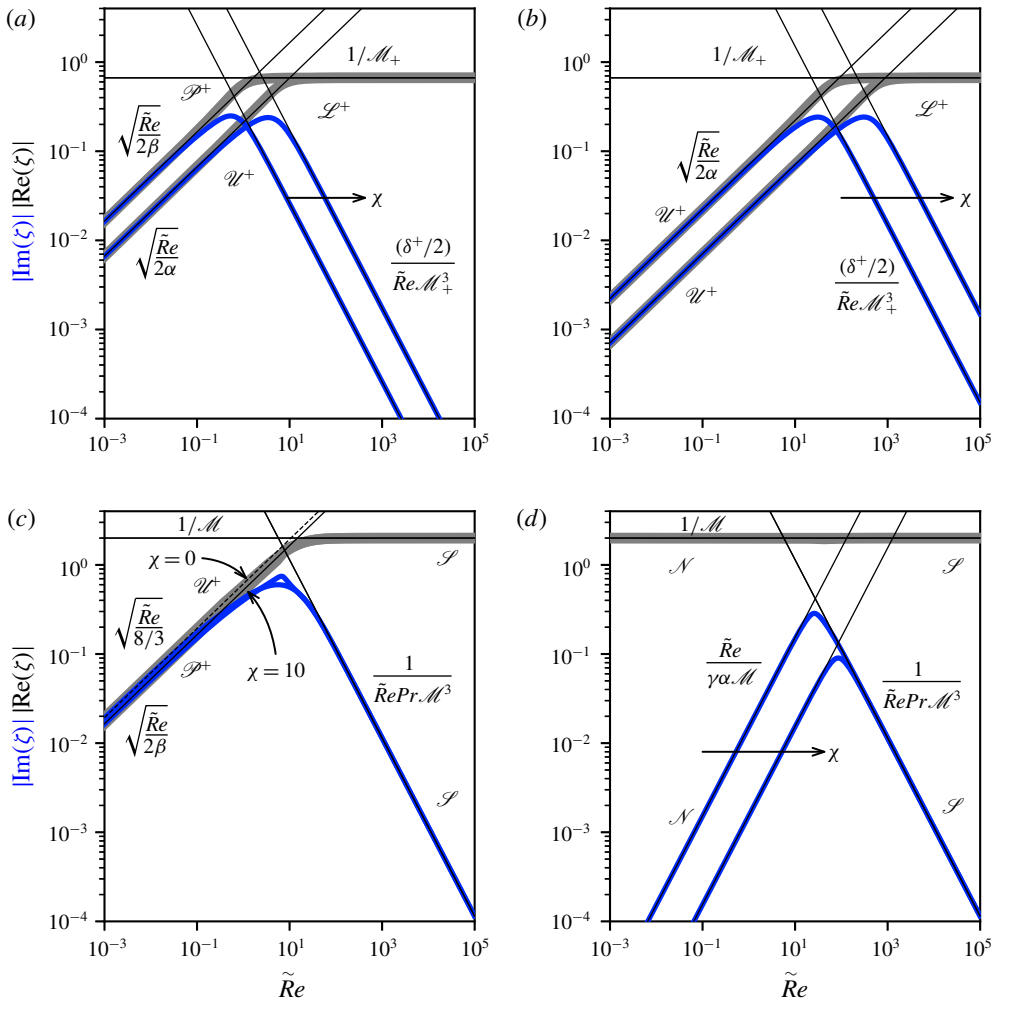

FIGURE 3. (Colour online) Magnitude of the real (thick grey) and imaginary (blue) parts of the wavenumber ζ along the $\mathscr{A}^+$ (*a*,*b*) and $\mathscr{E}$ (*c*,*d*) paths for $\chi \in \{0, 10\}$ (*a*,*c*) and $\chi \in \{10^2, 10^3\}$ (*b*,*d*), obtained from solving $\det(\boldsymbol{L}) = 0$. The solid and dashed black lines give the asymptotic solutions from §§ 2.1.2 and 2.1.3 (the scalings and the branch types are reproduced here for convenience).

on the sphere occurs in the Stokes regime. The effect of the damping factor on the fluctuating fields is therefore expected to be easier to read in the Landau regime (where the eigenvector is not changing much) than in the Stokes regime (where the fluctuating field will be influenced by both changes in the damping factor and variations in the eigenvector components). Apart from when it is connected to $\mathscr{U}^+$ ($\chi = 0$ case), the entropy path is seen to stay close to the equator of the sphere where $u = 0$. At high χ values the path becomes insensitive to the actual value of χ and sees its largest excursion in the Landau regime. Under such conditions, the fluctuating fields associated with the entropy path can therefore be directly anticipated from the properties of the damping factor. Specifically, pronounced density and pressure

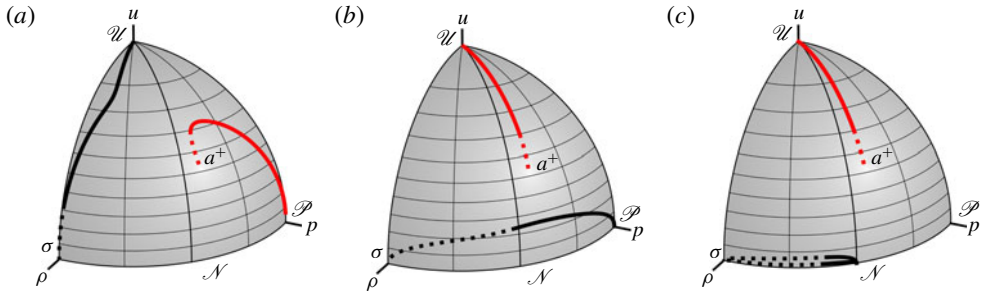

FIGURE 4. (Colour online) Eigenvector trajectories along the $\mathscr{A}^+$ (red) and $\mathscr{E}$ (black) paths for $\chi = 0$ (*a*), $\chi = 10$ (*b*) and $\chi \in \{10^2, 10^3\}$ (*c*) on the surface of one eighth of the unitary sphere in the Euclidean space formed by the dimensionless primitive variable. Since $\tilde{\boldsymbol{\mu}} \in \mathbb{C}^3$, the moduli of the components of $\tilde{\boldsymbol{\mu}}$ (divided by the magnitude of $\tilde{\boldsymbol{\mu}}$) are plotted instead (i.e. $(|\tilde{\rho}|, |\tilde{u}|, |\tilde{p}|)/\|\tilde{\boldsymbol{\mu}}\|$). Each path is split into the Stokes (solid line) and Landau (dotted line) regimes with the boundary defined as the $\tilde{Re}$ value for which $\mathrm{Im}(\zeta)$ in figure 3 reaches its maximum. All data are based on numerical solutions to (2.5). In the limit of $\tilde{Re} \to \infty$ the acoustic and entropy trajectories terminate on the a^+ and σ points, respectively. Once χ is sufficiently high for $\mathscr{U}^+$ to connect to $\mathscr{L}^+$ and $\mathscr{N}$ to connect to $\mathscr{S}$, the acoustic and entropy paths on the sphere vary very little when varying χ. In particular, the entropy path then lies near the equator (going from $\mathscr{N}$ to σ), and the acoustic path lies near the meridian connecting $\mathscr{U}^+$ to a^+.

fluctuations carried by the base flow are expected to arise when $\tilde{Re} \to 0$ (where $\mathrm{Im}(\zeta) \to 0$).

2.3. *The role of bulk viscosity in shaping the fluctuating field*

The variation of both the dispersion relation and the eigenvectors along all five continuous paths ($\mathscr{A}^\pm$, $\mathscr{E}$ and the remaining two Stokes branches) are now recombined to investigate their net effect on the fluctuating fields (again in the context of carbon dioxide with $\gamma = 1.29$, $Pr = 0.7$ flowing at $\mathscr{M} = 0.5$), defined as

$$\boldsymbol{\mu}_1 = \begin{bmatrix} \rho_0 & 0 & 0 \\ 0 & c_0 & 0 \\ 0 & 0 & p_0 \end{bmatrix} \mathrm{Im}\left\{ \sum_{n=1}^{5} \tilde{\boldsymbol{\mu}}_n \exp\left[\mathrm{i}\left(\omega t - k_n x + \varphi_n\right)\right] \right\}, \tag{2.15}$$

where the $(k_n, \tilde{\boldsymbol{\mu}}_n)$ pairs are the five solutions to (2.5). The eigenvectors, $\tilde{\boldsymbol{\mu}}_n$, are made unitary (based on the Euclidean norm) and the phase lags φ_n are chosen so as to align all $\tilde{u}$ components in the complex plane (to interpret as a forcing at $x = 0$ synchronised on the velocity fluctuation). Figure 5 gives the spatial evolution of the velocity fluctuations, combined with those of density, pressure and dilatational rate, for a range of acoustic Reynolds numbers, where space is made dimensionless using the acoustic wavelength, $\lambda_0 \equiv 2\pi c_0/\omega$.

A prominent feature of the fluctuating field is the existence of a range of acoustic Reynolds numbers over which perturbations are strongly damped and become rapidly negligible away from the source. This optimal (maximum) damping (see $\mathrm{Im}(\zeta)$ in figure 3) creates two distinctive 'quiet valleys' in the $\tilde{Re}$–$\tilde{x}$ maps (upstream and downstream of the source point) shown in figure 5. The position of each valley is governed by the intersection between the Stokes velocity-diffusion ($\mathscr{U}^\pm$) and the

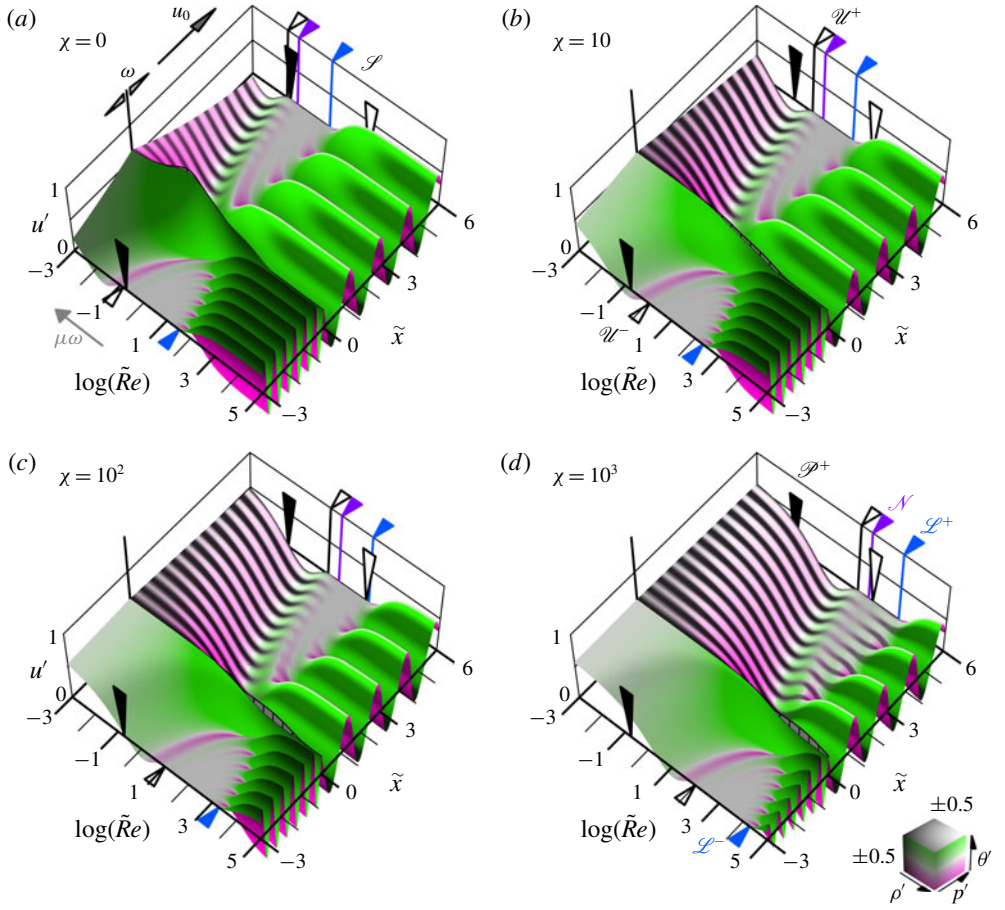

FIGURE 5. (Colour online) Spatial evolution of $u' \equiv u_1/c_0$ (where $\tilde{x} \equiv x/\lambda_0$ with $\lambda_0 \equiv 2\pi c_0/\omega$ is the distance in units of the Euler acoustic wavelength) based on (2.15) over a range of acoustic Reynolds numbers ($\tilde{Re}$) at time $tc_0/\lambda_0 = 0.1 \,(\mathrm{mod}\, 2\pi)$ (see Movie 1 for a full period), for $\chi \in \{0, 10, 10^2, 10^3\}$, $\gamma = 1.29$, $Pr = 0.7$ and $\mathscr{M} = u_0/c_0 = 0.5$. The lighting of the u' surface is such that positive density–pressure correlations are highlighted and coloured according to the dilatational rate (see colour scale for $\rho' \equiv \rho_1/\rho_0$, $p' \equiv p_1/p_0$, $\theta' \equiv \theta\lambda_0/c_0$). A triangular marker indicates the $\tilde{Re}$ location where one asymptotic-mode amplitude ($\mathscr{P}^{\pm}$, $\mathscr{U}^{\pm}$, $\mathscr{L}^{\pm}$, $\mathscr{N}$, $\mathscr{S}$) has dropped by 10 % from its $\tilde{x} = 0$ at the domain edge. Downward-pointing triangular markers correspond to χ-independent modes ($\mathscr{P}^{\pm}$, $\mathscr{S}$). Note the quiet regions (valleys) corresponding to the transition from the Landau to the Stokes regimes (when varying $\mu\omega$). The valleys shift to higher $\tilde{Re}$ values as χ is increased but is increasingly disturbed by ρ' from the fixed $\mathscr{S}$ branch. On the Stokes side of the valley, long (in λ_0 units) coherent structures in u'–θ' ($\mathscr{U}$) and p' ($\mathscr{P}$) structures combine downstream with the isothermal pressure–density fluctuations ($\mathscr{N}$ mode).

Landau acoustic-damping ($\mathscr{L}^{\pm}$) modes. The $\tilde{Re}$ intercept, $\tilde{Re}_{\mathrm{I}}$, can be seen from the asymptotic solutions to scale linearly with χ, i.e. $\tilde{Re}_{\mathrm{I}} \sim \chi$ if $\chi \gg 1$. This is indeed visible from the approximate shift of the valley by approximately one decade in $\tilde{Re}$ for each increment in χ of one order of magnitude. However, the shift of the

$\tilde{Re}$–$\tilde{x}$ map with χ is not self-similar owing to the fixed (χ independent) $\mathscr{P}^{\pm}$ and $\mathscr{S}$ branches. As χ is increased, the Landau entropy mode, $\mathscr{S}$, interferes with the valley (on the downstream side only) and the 'quiet' region bears its signature: more and more pronounced density fluctuations within the valley as χ increases. In the process, notice that χ provides a way to align the $\mathscr{L}^{+}$-mode damping with that of $\mathscr{S}$. In the configuration shown here, this alignment occurs for $\chi \sim 10^2$.

On the Stokes side of the valley (e.g. increasing $\mu\omega$ values), the transition into the $\mathscr{U}$ mode produces coherent structures on the dilatational rate extending many acoustic wavelengths (λ_0) away (see the coloured regions in figure 5 and Movie 1, which is available at https://doi.org/10.1017/jfm.2019.531). Based on the asymptotic results, the extent (λ) of these coherent structures scales according to $\lambda/\lambda_0 \sim (\chi/\tilde{Re})^{1/2}$ (for $\chi \gg 1$). This implies that high-χ fluid flows make the observation of a given large dilatational structure size (relative to the acoustic wavelength) possible at lower forcing frequencies (i.e. larger eddy sizes) than in the low- or zero-χ fluid. Superimposed to these coherent dilatational structures are coherent pressure–density fluctuations from the Newton mode, $\mathscr{N}$, downstream of the source point. These structures will be shown to play a major role in shaping turbulence in high-χ fluids.

3. Bulk-viscosity effects on small-scale two-dimensional turbulence

The eigenmode analysis presented in the previous section has thus revealed that whilst the bulk viscosity does not create new eigenmodes compared to those arising from the Navier–Stokes equations with $\chi = 0$, taking $\chi > 0$ provides a means to stretch the eigenmode landscape in non-self-similar and non-trivial manners. The stretching can expose properties of the eigenmodes that are usually out of reach when $\chi = 0$. For example, χ shifts the acoustic Landau damping towards larger Reynolds numbers, and thus eddy sizes. This means that χ can directly influence the acoustic-wave properties of the inertial range. This is precisely the observed effect in the very few dedicated studies (see § 1.2). However, shifting the Landau regime towards larger eddy sizes also implies that the Stokes regime is shifted towards the inertial range (it is hampered by viscous dissipation for $\chi = 0$ fluids, i.e. scales concerned by such regime would be sub-Kolmogorov, they have virtually no kinetic energy and are not resolved in practice). Given the peculiar nature of the eigenmodes in the Stokes regime (e.g. coherent dilatational structures spanning several acoustic wavelengths, isothermal density–pressure fluctuations) one expects those to influence the turbulence–kinetic-energy (TKE) redistribution. What would happen to the TKE redistribution if the quiet valleys from figure 5 are centred within the inertial range? This question is explored next.

3.1. *Computational strategy and initial conditions*

Numerical integrations of the Navier–Stokes equations (2.1) are performed using the in-house solver *CompReal* from Touber & Alferez (2019). The equations are integrated in time explicitly using a third-order total-variation-diminishing Runge–Kutta scheme (Shu & Osher 1989). Spatial derivatives are evaluated with a fourth-order centred finite difference dispersion-relation-preserving scheme (Tam & Webb 1993) using a thirteen-point stencil (a four points per wavelength cutoff is used for the dispersion optimisation process). The centred finite-difference scheme is stabilised using a centred thirteen-point eighth-order explicit discrete filter optimised in spectral space to minimise small-scale dissipation up to a cutoff wavenumber, following the methodology developed by Bogey & Bailly (2004) (a five points per

wavelength cutoff is used). This strategy accurately propagates large-wavelength content whilst minimising numerical errors at small scales (both from a dispersion and dissipation point of view), enabling, in particular, the study of acoustic waves down to wavelengths five times the grid spacing. Solutions to the Euler equations (i.e. setting $\mu = \mu_b = \kappa = 0$ in (2.1)) are also considered. These form discontinuities (eddy shocklets) and a shock-capturing strategy based on explicit localised artificial diffusivity (Cook & Cabot 2004) is employed. Artificial bulk viscosity and thermal conductivity are added to the momentum and energy equations where shocks are detected following the approach by Kawai, Shankar & Lele (2010). Detected discontinuities are redistributed across approximately four grid cells with spurious noise levels of approximately 1 % of the 'shock' strength (when coupled with accurate finite-difference operators).

Simulations of decaying homogeneous turbulence are performed in a two-dimensional periodic domain of size $L \times L$ (where L is an arbitrary length), discretised with $N \times N$ uniformly distributed points. The restriction to two-dimensional space is motivated by the associated reduction in computational cost (which, at best, scales linearly with χ) but also by the associated removal of the vortex-stretching mechanism, which will prove useful when highlighting a mechanism by which vorticity is promoted by μ_b that is also present in three-dimensional space (see § 3.5). A pseudo-dimensionless velocity field, $\boldsymbol{u}_o$, is derived by projecting its components drawn from a normal distribution onto a solenoidal field (based on the Helmholtz decomposition) and rescaled to the prescribed spectrum $E(\xi) = \beta\xi \exp[-(\xi/\xi_0)^2/2]$, where ξ is the dimensionless wavenumber ($\xi = L/\lambda$, where λ is the period of the wave of interest) and ξ_0 is a constant to prescribe. The constant β is adjusted to make the pseudo velocity field unitary, i.e. $\max(\boldsymbol{u}_o \cdot \boldsymbol{u}_o) = 1$. A pseudo-dimensionless pressure field, p_o, is then derived from $\boldsymbol{u}_o$ by solving the Poisson equation $\Delta p_o = -(\boldsymbol{\nabla u}_o)^\intercal : \boldsymbol{\nabla u}_o$ (where '$:$' is the contracted product; the Laplacian, Δ, and gradient, $\boldsymbol{\nabla}$, operators are rescaled by L^2 and L, respectively). A target thermodynamic state (ρ_0, p_0) is selected (this choice is arbitrary in ideal gases) and the pseudo-fields rescaled according to $p = p_0 + \rho_0 c_0^2 p_o$ and $\boldsymbol{u} = c_0 \boldsymbol{u}_o$, where $c_0^2 = \gamma p_0/\rho_0$ (c_0 is the isentropic ideal-gas sound speed evaluated at the target thermodynamic state). The temperature field is obtained from the equation of state assuming $\rho(\boldsymbol{x}, t = 0) = \rho_0$ (where $\boldsymbol{x}$ is the position vector). Thus, the initial velocity fluctuations are at most sonic and the initial kinetic energy is solely supplied to the solenoidal field. Most of the initial energy is concentrated around length scale $\ell = L/\xi_0$.

The initial condition is integrated in time using the Euler equations with shock capturing (E), the Navier–Stokes equations without (N) and with (B) bulk viscosity. Labels (E), (N) and (B) are used throughout the section to identify the set of equations used to provide the displayed result. Solutions using (N) and (B) are integrated only over a few energetic-eddy turnover times, whereas the Euler solution is integrated further.

3.2. *Choice of grid, fluid and flow properties in light of the linear theory results*

The strategy described above is applied to $N = 4128$, a choice which is representative of current high-end resolutions (i.e. number of point per characteristic length scale) achieved in three-dimensional direct numerical simulations of turbulence. The bulk (B) and no-bulk (N) viscosity cases are run at same Reynolds number, $Re \equiv \rho_0 U_0 L/\mu = 10^4\pi$, with $U_0 = c_0$ (i.e. the maximum speed at $t = 0$). The bulk-to-shear viscosity

ratio in case (B) is set to $\chi = 4 \times 10^3$ (recall that both μ and μ_b are kept constant and uniform).

Starting from the definition of the acoustic Reynolds number, $\tilde{Re} = \rho_0 c_0^2/(\mu\omega)$, and considering the dispersion relation $\omega = u_\phi \mathrm{Re}(k)$ (with $\mathrm{Re}(k) = 2\pi\xi/L$), one arrives at

$$\tilde{Re} = \frac{1}{2\pi\xi}\frac{Re}{\mathscr{M}_\phi \mathscr{M}_0}, \tag{3.1}$$

where $\mathscr{M}_0 \equiv U_0/c_0 = 1$ and $\mathscr{M}_\phi \equiv u_\phi/c_0$. Assuming $\mathscr{M}_\phi \sim 1$ (e.g. acoustic waves in a zero mean flow), equation (3.1) gives $\tilde{Re} \sim Re/(2\pi\xi)$. The smallest computed (but not resolved) scale $\lambda = L/N$ (giving $\xi = N$) provides a lower bound on the $\tilde{Re}$ scaling, i.e. $\tilde{Re} \sim Re/(2\pi N)$. Conversely, the largest computed scale $\lambda = L$ (giving $\xi = 1$) provides an upper bound, $\tilde{Re} \sim Re/(2\pi)$. For $Re = 10^4\pi$ and $N = 4128$, the simulation is thus expected to explore approximately four decades of acoustic Reynolds numbers centred around 10^2, i.e. $10^0 \lessapprox \tilde{Re} \lessapprox 10^4$.

The inherent finite range of resolved acoustic Reynolds numbers (from (3.1)) is put in regards to the linear theory results in figure 6 (and Movie 2) for both $\chi = 0$ and $\chi = 4 \times 10^3$ (with $\gamma = 1.29$, $Pr = 0.7$). Base-flow speeds ranging from $\mathscr{M} = 0$ to 1.2 are shown to illustrate the sensitivity of the $\tilde{Re}$–$\tilde{x}$ map to local flow-speed variations induced by large-scale eddies. The main idea here is that the quiet 'valleys' (§ 2.3) are positioned beyond the smallest resolved scales for the $\chi = 0$ case but towards the largest resolved scales for the non-zero-χ case. Therefore, whilst the zero-χ flow should be under the influence of the Landau damping towards the small scales, the non-zero-χ flow should exhibit a behaviour consistent with that of the Stokes regime at these same length scales. Based on the linear theory, the Stokes regime is characterised by the emergence of fast (supersonic, see $\mathscr{U}^\pm$ modes) large-scale contraction/expansion waves (large relative to the Euler acoustic wavelength, λ_0, at the same forcing frequency) on top of which positively correlated pressure–density perturbations propagate at the local flow speed. As the flow Mach number increases, so does the wavelength of these ρ'–p' (isothermal, see $\mathscr{N}$ mode) fluctuations, and the two structures form large (compared to λ_0) regions of in-phase ρ'–p'–θ' fluctuations (see higher $\mathscr{M}$ cases for the $\chi = 4 \times 10^3$ case in Movie 2). Such structures largely differ from the ρ'–p'–θ' fluctuations induced by acoustic waves (where θ' is always in phase opposition with respect to ρ' and p', see Movie 2, and the ρ'–p' fluctuations are at constant entropy and not temperature). The range of Mach numbers given in figure 6 and Movie 2 match the range of local Mach numbers obtained in the present turbulence simulations. The particular phase alignment of the ρ'–p'–θ' fluctuations in the Stokes regime will be shown to play a crucial role in enhancing solenoidal structures at small scales.

3.3. *Selective removal and promotion of turbulence structures by* μ_b

The initial condition described in § 3.1 is applied to $\xi_0 = 8$ (giving $\tilde{Re} \approx 6 \times 10^2$). This choice enables the observation of a dual cascade on the solenoidal velocity field (see Mininni & Pouquet 2013) of the Euler flow, which is deliberately centred in the vicinity of the transition into the Stokes regime of the high-bulk fluid case (i.e. $\mathcal{E} \sim \xi^{-3}$ for $\xi > \xi_0$, and $\mathcal{E} \sim \xi^{-5/3}$ for $\xi < \xi_0$, where $\mathcal{E}$ is the energy spectral density). Strictly speaking, the possibility of observing a double cascade is based on the existence of two quadratic invariants (i.e. the space-averaged kinetic energy and enstrophy, see Kraichnan 1967; Boffetta & Ecke 2012, for details) and is therefore

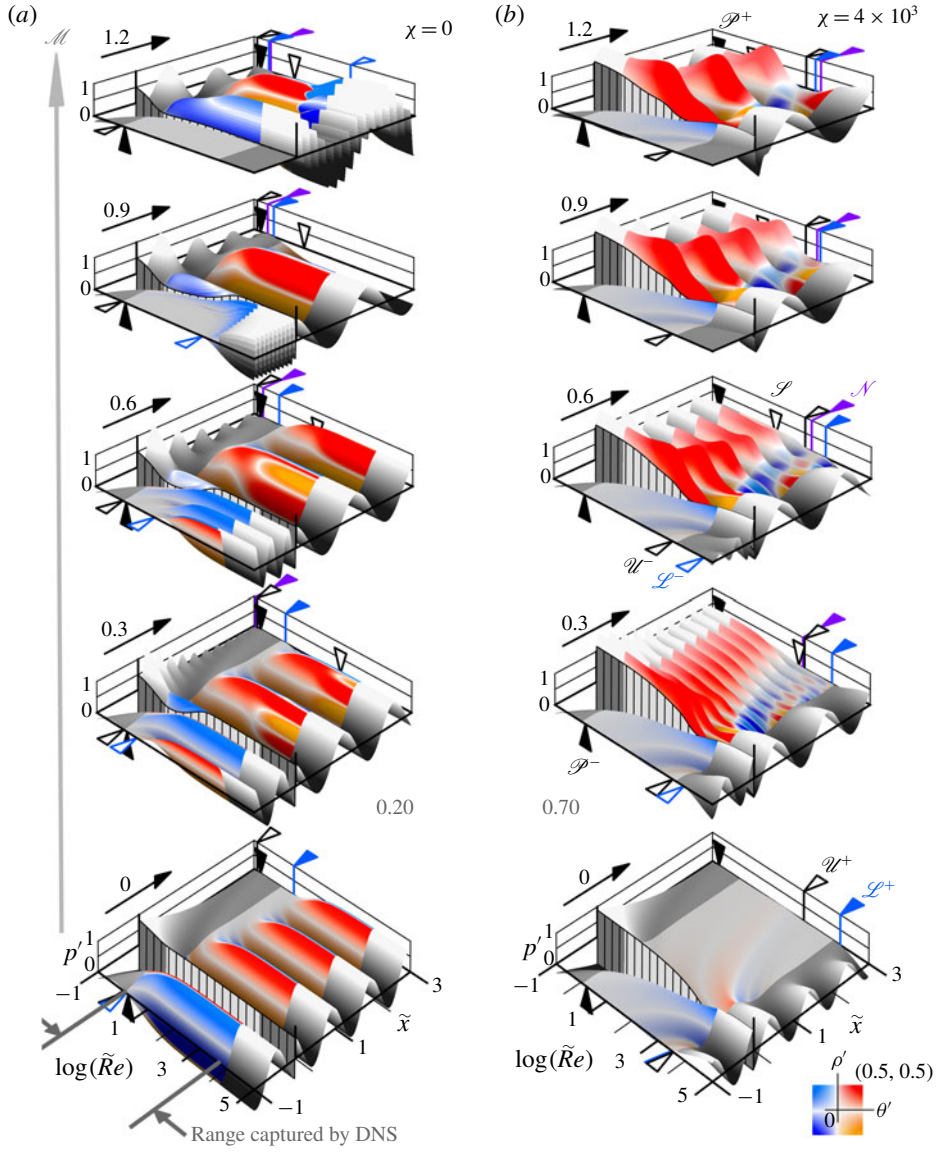

FIGURE 6. (Colour online) Spatial ($\tilde{x}$) evolution of p' over a range of acoustic Reynolds numbers ($\tilde{Re}$) for $\chi = 0$ (*a*) and $\chi = 4 \times 10^4$ (*b*) and $\mathscr{M} \in \{0, 0.3, 0.6, 0.9, 1.2\}$ (with $\gamma = 1.29$, $Pr = 0.7$). The lighting of the p' surface follows its signed magnitude and is coloured following θ'–ρ' correlations (see colour scale). The triangular markers position the 10 % drop in the asymptotic modes. See § 2.3 and figure 5 for details. Movie 2 gives a full forcing period. The light is deemed and the colouring off for $\tilde{Re}$ numbers *a priori* not captured by the current turbulence simulations. The $\chi > 0$ simulation is designed to observe Stokes regime within the inertial range.

restricted to incompressible (decaying) turbulence in the inviscid limit. Figure 7 gives the isotropic energy spectral density over 60 large-eddy turnover time units (U_0/L) extracted from the velocity field (t) and its projection onto the solenoidal (s) and

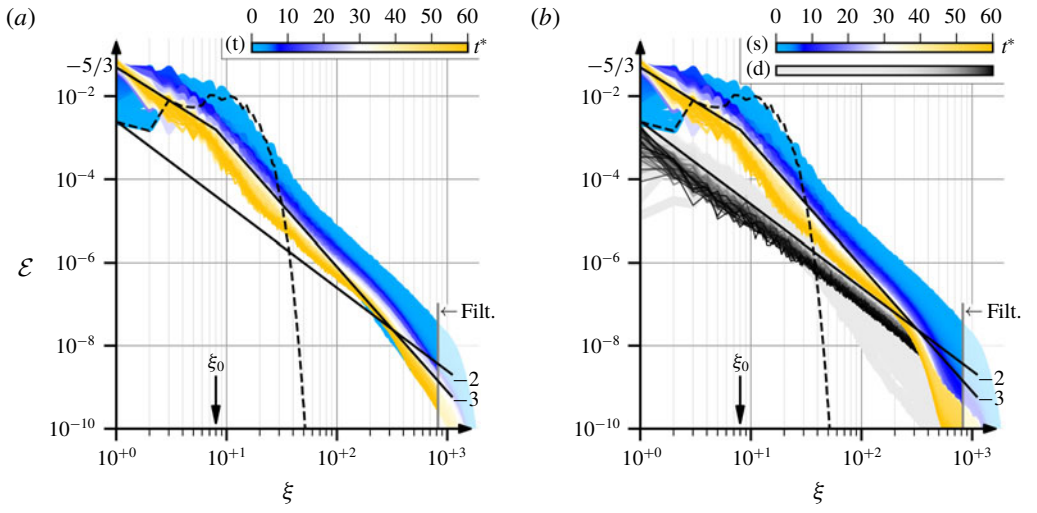

FIGURE 7. (Colour online) Isotropic energy spectral density ($\mathcal{E}$) of the total (t), solenoidal (s) and dilatational (d) velocity fields of the Euler simulation over the integration time $t^* \equiv tU_0/L \in [0, 60]$. The initial solenoidal energy deposition is shown in black dash line. The vertical line labelled 'Filt.' and transparent white patch indicate the range of wavenumbers explicitly filtered by the numerical method (grid with $N = 4128$ points). Both a direct enstrophy cascade ($\mathcal{E} \sim \xi^{-3}$ for $\xi > \xi_0$) and inverse energy cascade ($\mathcal{E} \sim \xi^{-5/3}$ for $\xi < \xi_0$) can be observed in the solenoidal field, with the direct cascade rapidly settling (times in light blue) compared to the inverse cascade (times in yellow). The dilatational field progressively assumes a Burgers-like spectrum ($\mathcal{E} \sim \xi^{-2}$). Owing to the difference in the direct cascade and Burgers-like spectral exponents (-3 versus -2), the solenoidal and dilatational energies becomes comparable at high wave numbers, where the classical exponents no longer hold. The total velocity displays a spectrum coinciding with the dominant contribution (i.e. mostly the solenoidal field here).

dilatational (d) components (following the Helmholtz decomposition). The solenoidal field is seen to follow the inviscid- and incompressible-flow theory, except for the noticeable decay in space-averaged kinetic energy (which is mostly converted here into internal energy by the artificial viscosity in eddy shocklets). The robustness of the incompressible-flow theory is rooted in the fact that most of the kinetic energy remains confined to the solenoidal modes (see Aluie 2011; Wang, Gotoh & Watanabe 2017; Wang *et al.* 2018, for examples), as can be seen from the dilatational kinetic energy, which assumes a Burgers-like spectrum (Gotoh 1994) with energy levels well below that of the solenoidal field (except at high wavenumbers, here $\xi > 3 \times 10^2$).

The robust and rapid establishment (in a couple of U_0/ℓ time units) of the enstrophy cascade is exploited here to seed the kinetic energy at high wavenumbers (i.e. $\xi > \xi_0$, down to the filter scale) in a manner which is representative of (two-dimensional) turbulence. These scales are expected to be under the influence of the Stokes regime. Figure 8 and Movie 3 give the spatial (and time) variations of the thermodynamic and mechanical pressures, the density, the temperature, the dilatational rate and the vorticity. The colouring is such that correlations in density and thermodynamic pressure are highlighted (white/blue regions correspond to in-phase pressure–density increases/decreases). The temperature field is shown in regards to such correlation, based on the mechanical pressure. This is to discriminate isothermal compressions

from the more usual isentropic compression, and therefore help to identify structures consistent with mode $\mathscr{N}$. The dilatational rate and vorticity fields illustrate the spatial (and temporal) distribution of both the dilatational and solenoidal kinetic energies.

The Euler-based (E) flow is characterised by a vortex-filamentation process down to the resolved scales (-3 enstrophy cascade), and the emission of acoustic waves over the same range of scales (which steepen to form shocks over time, -2 Burgers-like spectrum). Owing to the absence of transport coefficients, and except at shocks, fluid particles retain their initial entropy (set non-uniform, see § 3.1) and the temperature field captures both the filamentation process (advection by the local solenoidal flow) and the reversible local increases/decreases induced by passing acoustic waves (see Movie 3). Vortex cores are local pressure–density minima and induce stagnation points with local pressure–density maxima. The zero-χ (N) flow is similar to (E) and the two fields are in fact difficult to distinguish in the early times (see Movie 3). The departure from (E) is mostly visible at small scales, where the transport coefficients (set amongst the lowest possible for such computational grid) dissipate the kinetic energy: the vortex-filamentation process is limited to a physical scale by the shear viscosity (μ), and that of the temperature by thermal conductivity (κ); acoustic waves are increasingly damped towards small scales (expected Landau regime).

In contrast, the high-χ (B) flow is characterised by ρ'–p' structures resembling those of the vortex filaments. A closer look reveals that such structures are not visible in the temperature field, which remains similar to that of (N) – μ_b does not act directly on the temperature field. These structures therefore share the properties of the Newton eigenmode ($\mathscr{N}$). The $\mathscr{N}$ and $\mathscr{S}$ branches along the entropy path (see figure 3) intersect at $\tilde{Re} = [(4/3 + \chi)\gamma/Pr]^{1/2}/\mathscr{M}$, which for the highest $\mathscr{M} \sim 1.2$ values reached here translates to $\tilde{Re} \sim 70$. Structures with sizes similar or smaller than that given for $\tilde{Re} = 50$ in figure 8 are thus expected to be under the influence of the $\mathscr{N}$ mode (on the left of the quiet valley in figure 6). The dilatational field, although an order of magnitude smaller than for (N), is also found to follow the filamentary property of vorticity, and the vorticity field itself appears sharper than in (N). These remarks contradict the notion that more bulk viscosity necessarily imply that more small scales are damped. Acoustic waves are indeed absent in (B), see Movie 3, but other sharp structures emerge, which are borrowed from the Stokes regime (similarly to the notion that acoustic waves are borrowed from the Euler limit when dissipative processes become negligible).

Remarkably, the correlation between small-scale thermodynamic pressure structures and the dilatational field (expected from Stokes regime) gives the mechanical pressure field in (B) a topology that is similar to that of (E) and (N), see figure 8 and Movie 3, at the exception of acoustic-wave footprints, which are necessarily visible in the thermodynamic (and thus mechanical) pressure for (E) and (N) (but are absent in (B)). No footprint arising from Stokes regime is visible in p_m for (B). The time rate of change of the specific kinetic energy of a fluid particle (derived from (2.1)) is governed by

$$\rho \dot{e}_c = -\boldsymbol{u} \cdot \boldsymbol{\nabla} \left(p_m - \tfrac{1}{3}\mu\theta \right) + \mu \Delta e_c, \tag{3.2}$$

where $e_c \equiv \boldsymbol{u} \cdot \boldsymbol{u}/2$, $\dot{e}_c \equiv \partial e_c/\partial t + (\boldsymbol{u} \cdot \boldsymbol{\nabla}) e_c$, and assuming a uniform dynamic viscosity. With the mechanical pressure field deprived from both acoustic waves and Stokes structures, p_m assumes a topology reminiscent of that of incompressible flows (i.e. low values at vortex cores, see figure 8 and Movie 3). Thus, particles orbiting within isolated vortices are expected to experience pressure forces, $\boldsymbol{\nabla} p_m$, orthogonal to their

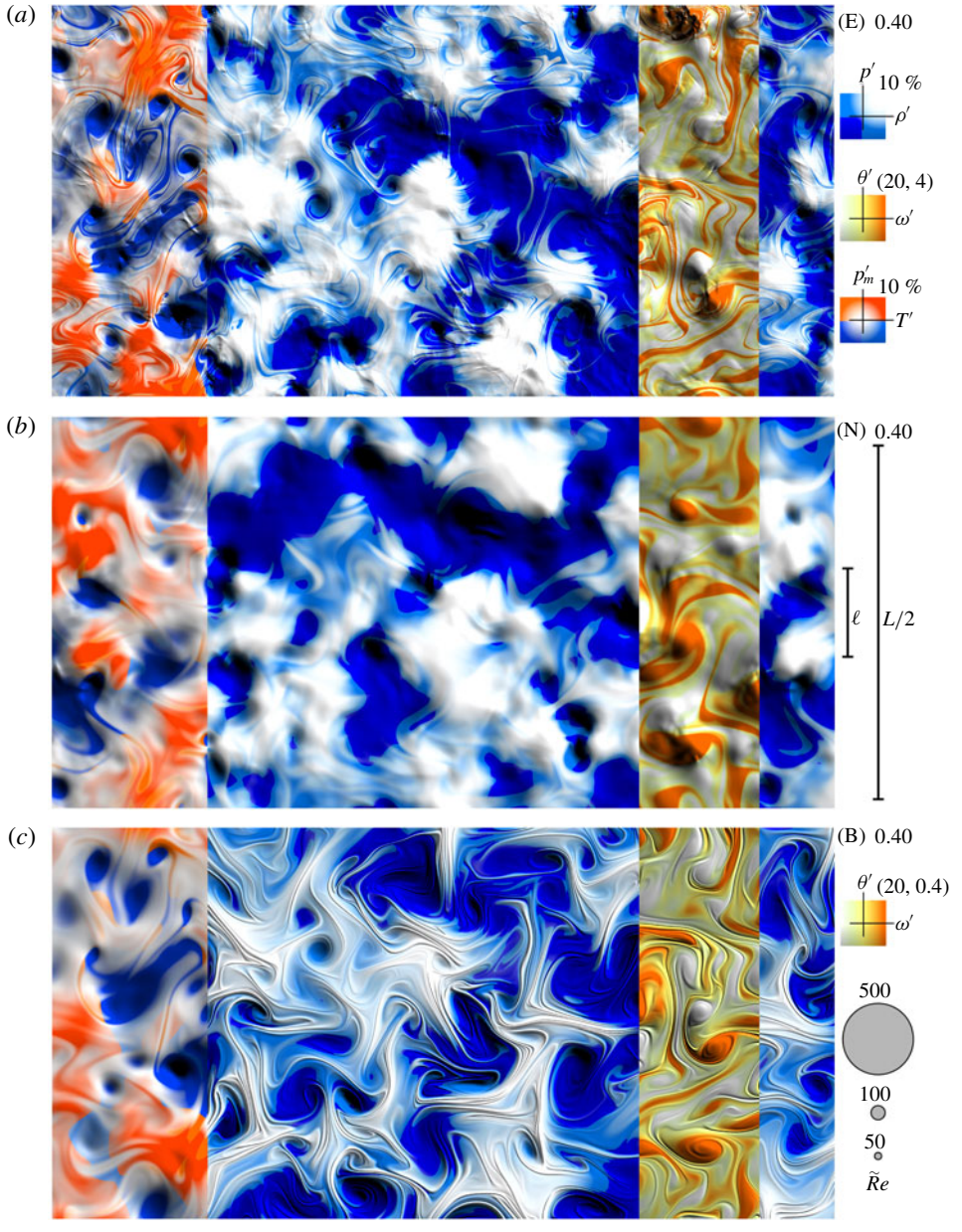

FIGURE 8. (Colour online) Pressure ($p' \equiv (p - p_0)/(\rho_0 c_0^2)$) and density ($\rho' \equiv (\rho - \rho_0)/\rho_0$) fluctuations (in blue–white) at $t^* \equiv tU_0/L = 0.4$ for cases (E), (N) and (B), with $\tilde{R}e$-scale estimates ((3.1) with $\mathscr{M}_\phi \mathscr{M}_0 = 1$). Narrow-band overlays give the mechanical pressure ($p'_m \equiv (p_m - p_0)/(\rho_0 c_0^2)$) and temperature ($T' \equiv (T - T_0)/T_0$) fluctuations (in blue-red), the dilatational rate ($\theta' \equiv \theta L/c_0$) and (positive) vorticity ($\omega' \equiv (L/c_0)(\boldsymbol{\nabla} \times \boldsymbol{u}) \cdot \boldsymbol{e}_z$) fields (in orange–white). Fields are tiled following the L-periodicity (in both vertical and horizontal directions). Lighting on p' placed on the top-right corner is applied for depth effect (dip at vortex core). Movie 3 provides a time animation of the above for $t^* \in [0, 0.5]$. Key remarks and interpretations are given in the text.

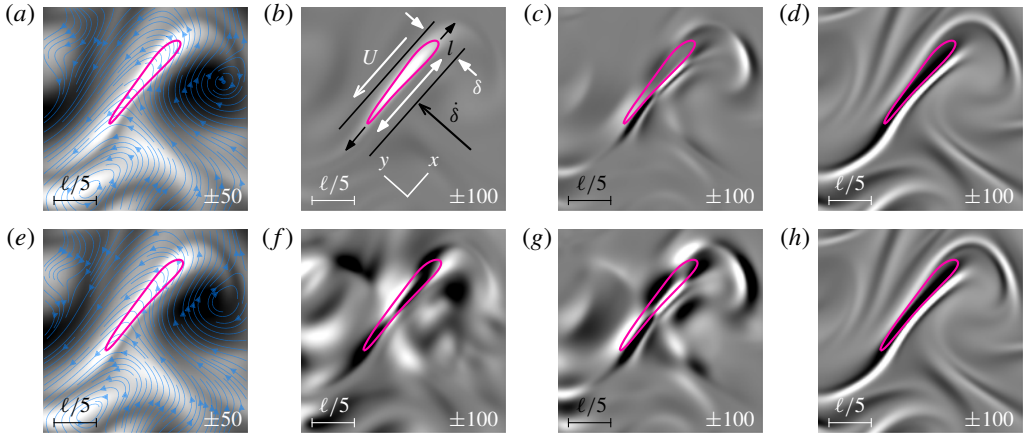

FIGURE 9. (Colour online) Vorticity enhancement along a vortex filament (see (3.4)). From left to right: Ω (normalised by U_0/L) (*a*,*e*); $-\Omega\theta$ (*b*,*f*), Π (*c*,*g*), $\nu\Delta\Omega$ (*d*,*h*) (all normalised by $(U_0/L)^2$); for case $\chi = 4\times10^3$ (*a*,*b*,*c*,*d*) and case $\chi = 0$ (*e*,*f*,*g*,*h*) $0.1\,U_0/L$ after initial release at $t = 0$ on the $N = 4128$ grid. The blue lines are streamlines with a thickness indicative of the velocity magnitude. Magenta contours give $\Omega L/U_0 = 65$. The grey scale is clipped according to the value at the bottom right corner of each image (with white for positive). In addition to the 'filamentation' process (responsible for the local growth in enstrophy), the vorticity-dilatation correlation ($\Omega\theta$ term) is seen to benefit from the Stokes-mode coherence to further contribute to the enstrophy production (in the no-bulk case, $\Omega\theta$ is less structured owing to the presence of acoustic waves and $|\Omega|$ is both enhanced and reduced within the filament). The intensity of the vorticity at small scales in the high-bulk fluid case is initially enhanced.

own velocities, $\boldsymbol{u}$, thereby producing no work, such that e_c remains constant. Similarly, particles cruising in between vortices, such as a contrarotating vortices, would first experience a pressure gradient in their direction of motion (speeding it up) followed by the opposite process (sometime leading to a stagnation point).

This picture is to contrast with the no-bulk calculation which is very much under the influence of the work done by compression/expansion processes due to the passage of acoustic waves (leading to an increase in friction work and viscous diffusion). Thus, the kinetic energy of high-χ fluid flows is not directly drained through an excess dissipation in acoustic waves (as may have been intuited). Instead, no acoustic wave is formed (in Stokes regime) and the absence of the small-scale structures from the Stokes mode in the mechanical pressure confers incompressible-like properties to the kinetic energy. This comment applies to the translational kinetic energy of a fluid particle.

The picture for the rotational kinetic energy (enstrophy) is different. The time rate of change of the vorticity of a fluid particle (derived from (2.1)) is governed by

$$\dot{\boldsymbol{\omega}} = (\boldsymbol{\omega}\cdot\boldsymbol{\nabla})\boldsymbol{u} - \theta\boldsymbol{\omega} - \boldsymbol{\nabla}\vartheta\times\boldsymbol{f} + \nu\Delta\boldsymbol{\omega}, \tag{3.3}$$

where $\boldsymbol{\omega}\equiv\boldsymbol{\nabla}\times\boldsymbol{u}$, $\dot{\boldsymbol{\omega}}\equiv\partial\boldsymbol{\omega}/\partial t + (\boldsymbol{u}\cdot\boldsymbol{\nabla})\boldsymbol{\omega}$, $\vartheta\equiv1/\rho$, $\boldsymbol{f}\equiv\boldsymbol{\nabla}(p_m - \mu\theta/3) - \mu\Delta\boldsymbol{u}$, $\nu\equiv\mu/\rho$, assuming uniform dynamic viscosity. The first term on the right-hand side of (3.3) is the vortex stretching term, which vanishes in two-dimensional space. The second term, $\theta\boldsymbol{\omega}$, plays a similar role (i.e. both terms express the conservation of angular momentum in the absence of external forces) and is still present in two-dimensional space (this

term is the fluid equivalent to the action of an ice skater drawing its arms inward when spinning). The third term is an extension to the baroclinic production term ($-\boldsymbol{\nabla}\vartheta \times \boldsymbol{\nabla}p$) and the last term corresponds to the diffusion of vorticity by the shear viscosity.

The contribution of each term on the right-hand side of (3.3) in the context of a two-dimensional vortex filament is given in figure 9. Considering the local Cartesian coordinates given in the figure, the projection of (3.3) on $\boldsymbol{e}_z$ gives

$$\underset{O(\Phi)}{\frac{\partial \Omega}{\partial t}} + \underset{O(\Phi\Upsilon\epsilon)}{u\frac{\partial \Omega}{\partial x}} + \underset{O(\Phi)}{v\frac{\partial \Omega}{\partial y}} = \underset{O(\Phi)}{-\Omega\theta} + \Pi + \underset{O(\Phi\Psi\epsilon^2)}{\nu\frac{\partial^2 \Omega}{\partial x^2}} + \underset{O(\Phi\Psi)}{\nu\frac{\partial^2 \Omega}{\partial y^2}}, \tag{3.4}$$

where $\Omega \equiv \boldsymbol{\omega}\cdot\boldsymbol{e}_z$, $\Pi \equiv -[\boldsymbol{\nabla}\vartheta \times \boldsymbol{f}]\cdot\boldsymbol{e}_z$, $\Phi \equiv U\dot{\delta}/\delta^2$, $\Upsilon \equiv U/\dot{\delta}$, $\epsilon \equiv \delta/l$, $\Psi \equiv \mu/(\rho_0\dot{\delta}\delta)$. The orders of magnitude are obtained considering $\Omega \sim U/\delta$, $\theta \sim \dot{\delta}/\delta$, $u \sim U$, $v \sim \dot{\delta}$ and a characteristic time $\delta/\dot{\delta}$. Since the filamentation process is induced by the energy-rich eddies from the initial condition, the shearing and squeezing speeds are $U \sim U_0$ and $\dot{\delta} \sim U_0$ (hence $\Upsilon \sim 1$). Moreover, let $\varphi \equiv L/\delta$, giving $\Phi = \varphi^2(U_0/L)^2$ and $\Psi = \varphi/Re$.

Initially, the vortex filament is a blob of vorticity with $\delta \sim l \sim \ell$, giving $\epsilon \sim 1$, $\varphi \sim \xi_0$, and $\Psi \sim \xi_0/Re \ll 1$. Thus, the time rate of change of the vorticity of a fluid particle within the vortex filament is initially under the influence of the vorticity dilatation and production terms, i.e. $\dot{\Omega} \approx -\Omega\theta + \Pi$. Assuming a constant compression rate $\theta < 0$, the homogeneous part of this last equation suggests that the vorticity of a fluid particle initially undergoes an exponential growth (for $\Omega > 0$ and $\theta < 0$ as in the configuration of figure 9), i.e. $\Omega \sim \Omega_{t=0}\exp(|\theta|t)$ (ignoring forcing from Π).

At later times, when the filament geometry is such that $\delta \ll l$, $l \sim \ell$ and $\epsilon Re \sim 1$, giving $\varphi = (L/l)\epsilon^{-1} \sim \epsilon^{-1}$, and $\Psi \sim (\epsilon Re)^{-1} \sim 1$, the time rate of change of vorticity of a fluid particle inside the filament ($\partial\Omega/\partial t + v\partial\Omega/\partial y$) is under the competing influence of the enhancement due to the vorticity-dilatation correlation ($-\Omega\theta$) and viscous diffusion ($\nu\partial^2\Omega/\partial y^2$), again ignoring Π for now. This is essentially the time captured in figure 9. The filamentation ceases when the diffusion term eventually dominates every other term ($\Psi \gg 1$).

From these considerations on the vorticity equation, the vorticity-dilatation term can clearly play a significant role in the enhancement of Ω during the early stages of the filamentation process (which is the main driver for the enstrophy cascade, see chapter 10 in Davidson 2004, for example). The high-bulk flow benefits from the strong correlation between Ω and θ (which is related to Stokes regime). There is no definite vorticity-dilatation correlation in the no-bulk flow (which is entirely in the Landau regime) since the dilatational field is mostly due to acoustic waves travelling through the vortex filaments, thereby both promoting and reducing Ω with no net effect (see figure 9*f*). Term Π does not contribute much to the balance inside the filament shown in figure 9 in the high-bulk fluid case, and whilst more active in the no-bulk case, its contribution does not lead to a net effect (both signs occur within the structure).

3.4. *Spectral signature*

The statistical importance of the structures discussed previously are now assessed in the energy spectra. Figure 10 gives the isotropic spectral density of the velocity fields projected onto solenoidal ($\mathcal{E}_s$) and dilatational ($\mathcal{E}_d$) components over $2.4\ell/U_0$ from the initial solenoidal kinetic-energy injection at $\xi = 8$ (downward triangular marker in $\mathcal{E}_s$ plot). The enstrophy 'cascade' is responsible for the rapid establishment of

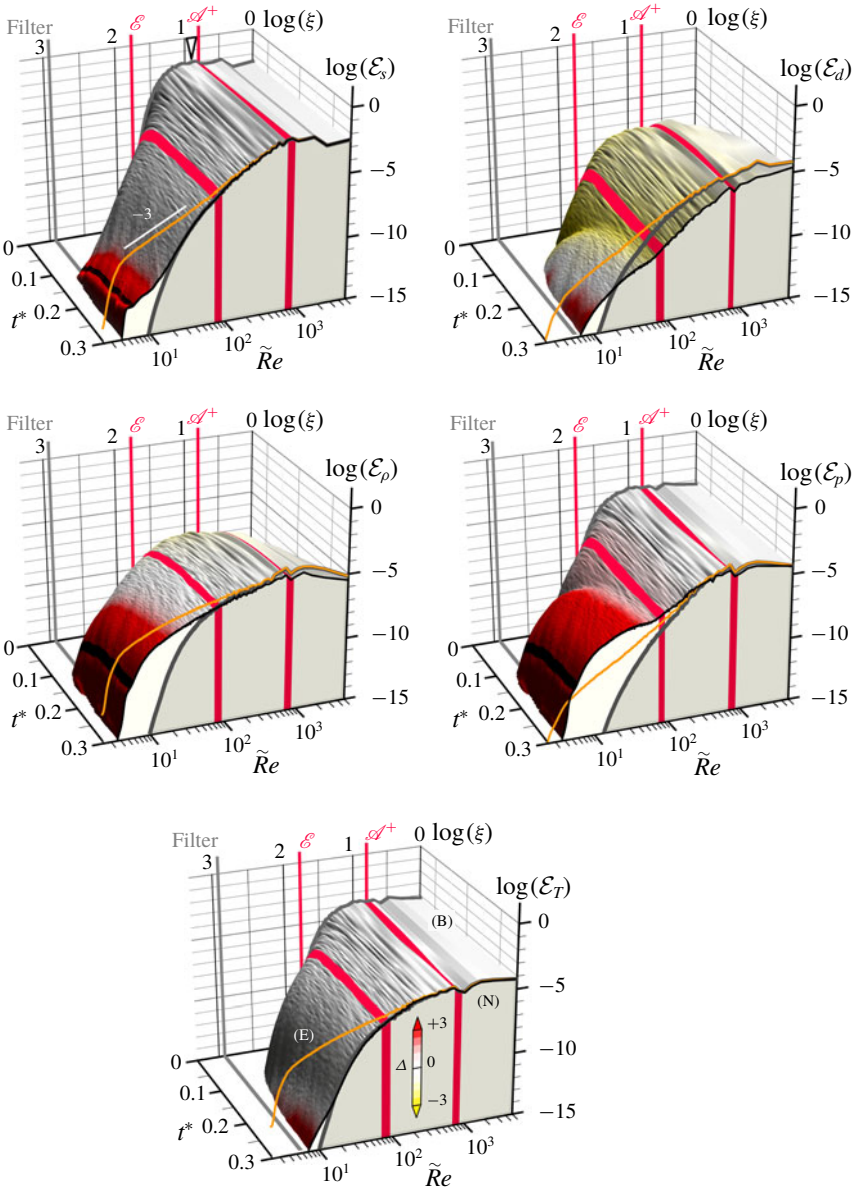

FIGURE 10. (Colour online) Isotropic energy spectral density at $t^* \in [0, 0.3]$ for the solenoidal ($\mathcal{E}_s$) and dilatational ($\mathcal{E}_d$) velocity fields, and isotropic 'energy' spectral density for pressure ($\mathcal{E}_p$), density ($\mathcal{E}_\rho$) and temperature ($\mathcal{E}_T$) for case (B), coloured according to $\Delta \equiv \log(\mathcal{E}^{\chi\neq 0}) - \log(\mathcal{E}^{\chi=0})$, with a lighting based on the slope of $\log(\mathcal{E}^{\chi\neq 0})$ with the light source placed above (darker implies steeper). The Euler (E) spectrum is shown in orange only at $t^* = 0.3$. The $\tilde{Re}$ axis is computed from (3.1) with $Re = 10^4\pi$, $\mathscr{M}_\phi\mathscr{M}_0 = 1$. A dark 'ribbon' is applied where the spectrum reaches scales explicitly altered by the filter. Two red 'ribbons' mark where the entropy ($\mathscr{E}$) and acoustic ($\mathscr{A}^+$) paths reach their maximum damping (see figure 3) for $\mathscr{M} = 1$.

the $\mathcal{E}_s \sim \xi^{-3}$ spectrum in (E), which is eroded (with no clear spectral exponent) at small scales in (N) owing to the work done by friction (μ acts on both shearing and compression/expansion motions), irreversibly converting the kinetic energy into internal energy (heat here). Some of the initial solenoidal kinetic energy is transferred to the dilatational kinetic energy following the emission of acoustic waves (and formation of eddy shocklets). Since the smallest resolved scales in (N) fall within the Landau regime (see figure 6), acoustic waves are increasingly damped at small scales and $\mathcal{E}_d$ rolls off before (in terms of ξ values) reaching the scales explicitly removed by the filter.

In contrast, the high-χ case (B) exhibits a drop (relative to (N)) of two orders of magnitude in the dilatational kinetic energy for $\xi \in [10, 80]$, corresponding to a range of $\tilde{Re}$ values near the estimated optimal damping along the acoustic paths $\mathscr{A}^{\pm}$ (see § 2.3 and $\mathscr{A}^{+}$ marker in figure 10), where the transfer of the supplied solenoidal kinetic energy to the dilatational kinetic energy (via acoustic waves) is expected to be impaired. Consistent with this observation, scales coinciding with the emergence of Stokes regime experience easier transfers into dilatational kinetic energy (see the hump in $\mathcal{E}_d$ at $\tilde{Re} \sim 10^2$). These transfers are no longer acoustic in nature (as discussed previously) but are associated with the Stokes eigenmode, $\mathscr{U}$, which prevails here by design. Together with the Newton mode, $\mathscr{N}$ (present so long a local flow exists), the flow is now characterised by in-phase ρ–p–θ fluctuations which act to enhance the vorticity of vortex filaments (via vorticity-dilatation correlation, as discussed). This process increases the solenoidal kinetic energy contained at small scales (see the pronounced hump in $\mathcal{E}_s$ for (B), with energy levels exceeding those of (N) by more than three orders of magnitude).

Moving to the thermodynamic variables (figure 10), the pressure spectrum ($\mathcal{E}_p$) develops a prominent hump with levels around the $\tilde{Re} = 10$ mark exceeding those of (E) and (N) by four and five orders of magnitude, respectively. These scales correspond to the filamentary p' structures in figure 8 and Movie 3. Unlike for cases (E) and (N), the amplitude of the $\mathcal{E}_p$ spectrum at high wavenumbers in (B) is not acoustic in nature (see $\mathscr{P}$ and $\mathscr{N}$ eigenmodes), as the hump strikingly emerges on the Stokes side of the entropy path, $\mathscr{E}$ (see the marker indicating the optimal-damping position along the entropy path in figure 10). A similar observation applies to the density spectrum ($\mathcal{E}_\rho$), though not exceeding the energy levels from (E), consistently with the absence of ρ' contributions on modes $\mathscr{P}^{\pm}$. Remarkably, the temperature spectra ($\mathcal{E}_T$) are nearly identical between (B) and (N) for an extended time (this is made visible by the absence of yellow/red colours), as was anticipated from Movie 3. Isothermal compressions are consistent with the Newton-eigenmode properties, characterised by in-phase ρ–p fluctuations advected at the local flow speed and least damped at low $\tilde{Re}$ (the damping factor scales linearly with $\tilde{Re}$, see (2.14) for details). At later times, a small hump develops on $\mathcal{E}_T$ as a consequence of the excess solenoidal energy at high wavenumbers. Indeed, vorticity filaments produce heat by friction work (μ) and the generated heat is diffused by thermal conductivity (κ), conferring the small hump in the temperature spectrum (i.e. inherited from the solenoidal kinetic-energy spectrum).

The above observations lead to a word of caution about numerical simulations of high-χ fluid flows. The choice of grid resolution (N) and Reynolds number (Re) is traditionally set so that the energy at small scales is drained by the shear viscosity and not the filter or the regularisation method employed (such solution is said to be grid converged). This is the case for (N) in figure 10 (naturally, Euler simulations are never grid converged and always stabilised artificially, here with shock capturing

and filtering). However, when solving high-χ fluid flows, the setup must also take into account the transfer of solenoidal kinetic energy to the smallest computed scales (via the Stokes regime, as discussed in the present work). Evidence of the increased work done by the filter in case (B) is for example visible from the bright plateau past the filter scale in $\mathcal{E}_s$ (figure 10). Thus, not only the simulation time step must be adjusted to satisfy the viscous stability constraint, the mesh size must also be adjusted to capture this physical energy transfer to small scales. Both constraints have increased the simulation cost (in terms of time step size) of the present study by a factor 10^4 when compared to a similar study looking only at (N) and (E). Thus, whilst simulations of decaying turbulence on $(4128)^3$ grid points are feasible on national computing facilities, the required number of time steps to cover a few eddy turnover times is still prohibitive.

3.5. *Implications to three-dimensional turbulence*

The ability of bulk viscosity to shape small-scale turbulence structures was demonstrated here in two-dimensional space, and the mechanisms at play based on a one-dimensional linear-mode analysis. The significance of these arguments to more practical three-dimensional flows is on a par with arguments relating to the relevance of acoustic waves in three-dimensional turbulent flows, which are derived from one-dimensional linear modes of strictly non-dissipative fluids. In the same spirit, the transition to Stokes regime, whilst anticipated in one dimension, remains relevant to multiple dimensions. This is demonstrated here by the ability to predict its occurrence in two-dimensional flows, despite fluctuation levels of the order of 10 % of the base-flow properties. Thus, eigenmodes such as $\mathscr{U}^{\pm}$, $\mathscr{P}^{\pm}$ and $\mathscr{N}$ will survive a further dimensional increase, just like eigenmodes $a^{\pm}$, σ, $\mathscr{S}$ and $\mathscr{L}^{\pm}$ are still observed in three-dimensional flows (see Donzis & Jagannathan 2016; Pan & Johnsen 2017; Wang *et al.* 2018, for examples). Additional modes emerge when increasing the dimensional space, such as shear (vorticity) waves, the bedrock of turbulence. In the nonlinear regime, these modes do interact, and the resulting flow can still be interpreted in the eigenmode basis (and more generally, the linear part of the Navier–Stokes operator is known to predict turbulence structures such as streaks, see Blesbois *et al.* 2013, and references therein). In this work, a particular and significant (at least in two dimensions) interaction was shown to promote small-scale solenoidal motions, namely, the promotion of shear waves by dilatational modes (through the product of ω' with θ', which displays high levels of correlation in the Stokes regime over many acoustic wavelengths). Whether this particular mechanism dominates over vortex stretching (see (3.3)) remains an open question, but its existence is certain, and the present work provides practical scalings, based on asymptotic solutions, to assess whether a given flow is capable of capturing the Stokes regime (by computing branch intersects in figure 3 for example) and expected associated properties. Whilst bulk viscosity is shown to facilitate the observation of the Stokes regime, by shifting it towards the inertial range, the regime itself is also present in zero-bulk fluids, and the results shown here may be of interest to studies dedicated to dissipative scales (see Khurshid, Donzis & Sreenivasan 2018, for example). Early attempts in turbulent Couette flows (Szemberg O'Connor 2018) at $\chi = 10^3$, where the kinetic energy is supplied at large scales and on the solenoidal modes only, indicate that the dilatational structures discussed here in two dimensions do form within vortex sheets and promote the solenoidal kinetic energy at small scales (unpublished work).

4. Summary and concluding remarks

Intricate roles played by bulk viscosity on the dynamical properties of Newtonian-fluid flows were demonstrated analytically based on the eigenmodes of the one-dimensional Navier–Stokes equations. The existence of a continuous path in acoustic Reynolds number $\tilde{Re} = \rho_0 c_0^2/(\mu\omega)$ connecting the Euler regime of undamped acoustic and entropy modes (for $\tilde{Re} \to \infty$) to fast diffusive-dilatational (Stokesian) and advected isothermal-compression (Newtonian) modes (for $\tilde{Re} \to 0$) was established. The upper limit of the transition between the two regimes ($\tilde{Re} \gg 1$) coincides with the results by Landau (e.g. increased damping of acoustic waves with increasing μ and/or ω), the very foundation of the widespread view that transport coefficients (μ, μ_b and κ) act to damp the acoustic waves (and this effect is indeed exploited to deduce μ_b in laboratory experiments).

The Landau-damping view is in fact incomplete since it is limited in $\tilde{Re}$ range, owing to the emergence of the Stokes–Newton modes at low $\tilde{Re}$ values introduced in this work. Thus, there exists a maximum wave damping in $\tilde{Re}$ where both acoustic and entropy waves loose their identities and progressively assume properties resembling those of the Stokesian–Newtonian modes. Remarkably, the bulk viscosity is found to provide a convenient means to stretch the $\tilde{Re}$ coordinates. It is therefore possible to slide the optimum damping along the $\tilde{Re}$ axis via a change of μ_b (keeping everything else the same). In practice, this means that the Landau-to-Stokes transition can be placed in the inertial range of the turbulence kinetic-energy cascade, especially in carbon dioxide flows (where μ_b/μ is large enough to operate a significant shift along the $\tilde{Re}$ axis).

Overlaps between the inertial range and the Stokesian–Newtonian regime give rise to significant modifications of turbulence at small scales. First, because no acoustic wave may form or survive in this regime (cutting short the Burgers-like spectrum). Second, because the thinning process of vortical structures (by nearby eddies and vortex stretching) is found to be in phase with compression waves (of Stokesian–Newtonian origin, not of acoustic nature), leading to an increase of enstrophy at small scales (via the vorticity-dilatation correlation term). Solenoidal kinetic energy injected within the inertial range is therefore rapidly transferred to small scales, and then dissipated by friction work. Although the outcome may be consistent with the widespread intuition (i.e. bulk viscosity speeds up the dissipation of kinetic energy, the Landau-damping view), the path described in this work is notably different: it does not require any acoustic waves, is non-local in spectral space, and is ultimately achieved by the shear viscosity following the increase of enstrophy at small (dissipative) scales.

Whilst the identification of the Stokes–Newton and Landau–Euler regimes rests on the assumption of one-dimensional and linearised flows, the regimes (and associated eigenmodes) are still relevant to three-dimensional flows, in the same way acoustic waves remain relevant to three-dimensional compressible turbulence despite being initially extracted from an inviscid and linearised one-dimensional flow assumption. Unsurprisingly, the two-dimensional turbulence presented here displays features consistent with the predictions obtained from the linearised one-dimensional flow analysis, in particular the emergence of fast diffusive-dilatational and advected isothermal-compression modes above a target wavenumber that act to enhance the enstrophy at small scales.

Consequently, the proposed theory offers a convenient map to guide future numerical and laboratory experiments dedicated to the study of bulk-viscosity effects

on turbulence, as well as to provide insights into the interpretation of past results. In effect, the only study dedicated to bulk-viscosity effects on turbulence to date is that of Pan & Johnsen (2017), where the authors report (in the context of decaying turbulence) an increase in the decay rate of the turbulence kinetic energy by bulk viscosity with no noticeable change to the enstrophy. Their observations are consistent with the Landau regime (i.e. bulk viscosity dissipates the kinetic energy carried by the acoustic waves). Interestingly, the energy spectra at $\chi = 10^3$ appear to develop small humps at high wavenumbers (referred to as 'energy pile up' by the authors), suggesting that the smallest resolved scales ($N = 256$ in their simulations) are about to penetrate the Stokes regime. More resolved simulations would enable the Stokesian dilatational modes (not acoustic waves) to emerge and interfere with the enstrophy. Future studies (both numerical and experimental in nature) should consider this possibility, especially if the kinetic energy is continuously injected at large scales (via body forces or wall motion) since the resulting excess in enstrophy production at small scales is inevitably going to modify friction losses, and therefore heat-transfer properties. This is particularly relevant to engineering devices operating in carbon dioxide where this effect is not accounted for in the design, e.g. for more accurate predictions of aerothermal loads on exploratory systems for planet Mars, entropy losses in turbomachinery components and heat-exchanger performance in power plants operating on CO_2 (supercritical cycles for concentrated solar power for example).

Acknowledgements

This work has received support from the UK Engineering and Physical Sciences Research Council (EPSRC) (grant nos EP/L021676/1, EP/K503733/1), the UK Turbulence Consortium (grant no. EP/L000261/1), Imperial College Research Computing Service doi:10.14469/hpc/2232, and the Grantham Institute at Imperial College.

Supplementary movies

Supplementary movies are available at https://doi.org/10.1017/jfm.2019.531.

REFERENCES

ALFEREZ, N. & TOUBER, E. 2017 One-dimensional refraction properties of compression shocks in non-ideal gases. *J. Fluid Mech.* **814**, 185–221.

ALUIE, H. 2011 Compressible turbulence: the cascade and its locality. *Phys. Rev. Lett.* **106**, 174502.

ARIS, R. 1989 *Vectors, Tensors, and the Basic Equations of Fluid Mechanics*, 1st edn. Dover.

ASH, R., ZUCKERWAR, A. & ZHENG, Z. 1991 Second coefficient of viscosity in air. *NASA Tech. Rep.* CR-187783.

BLESBOIS, O., CHERNYSHENKO, S., TOUBER, E. & LESCHZINER, M. 2013 Pattern prediction by linear analysis of turbulent flow with drag reduction by wall oscillation. *J. Fluid Mech.* **724**, 607–641.

BOFFETTA, G. & ECKE, R. E. 2012 Two-dimensional turbulence. *Annu. Rev. Fluid Mech.* **44**, 427–451.

BOGEY, C. & BAILLY, C. 2004 A family of low dispersive and low dissipative explicit schemes for flow and noise computations. *J. Comput. Phys.* **194**, 194–214.

BOUKHARFANE, R. 2018 Contribution à la simulation numérique d'écoulements turbulents compressibles canoniques. PhD thesis, Ecole Nationale Supérieure de Mécanique et d'Aérotechnique – Poitiers.

COOK, A. W. & CABOT, W. H. 2004 A high-wavenumber viscosity for high-resolution numerical methods. *J. Comput. Phys.* **195**, 594–601.

CRAMER, M. S. & BAHMANI, F. 2014 Effect of large bulk viscosity on large-Reynolds-number flows. *J. Fluid Mech.* **751**, 142–163.

CRAMER, M. S. 2012 Numerical estimates for the bulk viscosity of ideal gases. *Phys. Fluids* **24**, 1–23.

DAVIDSON, P. A. 2004 *Turbulence: An Introduction for Scientists and Engineers*. Oxford University Press.

DONZIS, D. & JAGANNATHAN, S. 2016 Reynolds and Mach number scaling in solenoidally-forced compressible turbulence using high-resolution direct numerical simulations. *J. Fluid Mech.* **789**, 669–707.

GOTOH, T. 1994 Inertial range statistics of Burgers turbulence. *Phys. Fluids* **6** (12), 3985–3998.

GRAVES, R. & ARGROW, B. 1999 Bulk viscosity: past to present. *J. Thermophys. Heat Transfer* **13** (3), 337–342.

JAEGER, F., MATAR, O. K. & MÜLLER, E. A. 2018 Bulk viscosity of molecular fluids. *J. Chem. Phys.* **148**, 1–12.

KAWAI, S., SHANKAR, S. K. & LELE, S. K. 2010 Assessment of localized artificial diffusivity scheme for large-eddy simulation of compressible turbulent flows. *J. Comput. Phys.* **229** (5), 1739–1762.

KHURSHID, S., DONZIS, D. & SREENIVASAN, R. 2018 Energy spectrum in the dissipation range. *Phys. Rev. Fluids* **3**, 082601(R).

KOSUGE, S. & AOKI, K. 2018 Shock-wave structure for a polyatomic gas with large bulk viscosity. *Phys. Rev. Fluids* **3**, 1–42.

KOVÁSZNAY, L. S. G. 1953 Turbulence in supersonic flow. *J. Aeronaut. Sci.* **20**, 657–674.

KRAICHNAN, R. H. 1967 Inertial ranges in two-dimensional turbulence. *Phys. Fluids* **10** (7), 1417–1423.

LANDAU, L. D. & LIFSHITZ, E. M. 1987 *Fluid Mechanics*. Elsevier Science.

LELE, S. K. 1994 Compressibility effects on turbulence. *Annu. Rev. Fluid Mech.* **26**, 211–254.

LIAO, W., PENG, Y. & LUO, L.-S. 2009 Gas-kinetic schemes for direct numerical simulations of compressible homogeneous turbulence. *Phys. Rev.* E **80**, 046702 1–26.

MEADOR, W., MINER, G. & TOWNSEND, L. 1996 Bulk viscosity as a relaxation parameter: fact or fiction? *Phys. Fluids* **8** (1), 258–261.

MININNI, P. D. & POUQUET, A. 2013 Inverse cascade behavior in freely decaying two-dimensional fluid turbulence. *Phys. Rev.* E **87**.

PAN, S. & JOHNSEN, E. 2017 The role of bulk viscosity on the decay of compressible, homogeneous, isotropic turbulence. *J. Fluid Mech.* **833**, 717–744.

PHILLIPS, E. M. & STELLA, V. J. 1993 Rapid expansion from supercritical solutions: application to pharmaceutical processes. *Intl J. Pharm.* **94**, 1–10.

RINALDI, E., PECNIK, R. & COLONNA, P. 2015 Computational fluid dynamic simulation of a supercritical CO_2 compressor performance map. *Trans. ASME J. Engng Gas Turbines Power* **137**, 1–7.

SCIACOVELLI, L., CINNELLA, P. & GLOERFELT, X. 2017 Direct numerical simulations of supersonic turbulent channel flows of dense gases. *J. Fluid Mech.* **821**, 153–199.

SHU, C.-W. & OSHER, S. 1989 Efficient implementation of essentially non-oscillatory shock capturing schemes, II. *J. Comput. Phys.* **83**, 32–78.

STOKES, G. G. 1845 On the theories of the internal friction of fluids in motion, and of the equilibrium and motion of elastic solids. *Trans. Camb. Phil. Soc.* **8**, 287–319.

SZEMBERG O'CONNOR, T. 2018 Bulk viscosity effects in compressible turbulent Couette flow. PhD thesis, Imperial College London.

TAM, C. K. W. & WEBB, J. C. 1993 Dispersion-relation-preserving finite difference schemes for computational acoustics. *J. Comput. Phys.* **107**, 262–281.

TOUBER, E. & ALFEREZ, N. 2019 Shock-induced energy conversion of entropy in non-ideal fluids. *J. Fluid Mech.* **864**, 807–847.

WANG, J., GOTOH, T. & WATANABE, T. 2017 Spectra and statistics in compressible isotropic turbulence. *Phys. Rev. Fluids* **2**.

WANG, J., WAN, M., CHEN, S. & CHEN, S. 2018 Kinetic energy transfer in compressible isotropic turbulence. *J. Fluid Mech.* **841**, 581–613.

WRIGHT, M. J., TANG, C. Y., EDQUIST, K. T., HOLLIS, B. R., KRASA, P. & CAMPBELL, C. A. 2010 A review of aerothermal modeling for Mars entry missions. In *48th AIAA Aerospace Sciences Meeting Including the New Horizons Forum and Aerospace Exposition* AIAA 2010-0443. AIAA.